atmosphere

Article

Energy Partitioning and Air Temperature Anomalies Above Urban Surfaces: A High-Resolution PALM-4U Study

Daniela Cava [1,*], Luca Mortarini [2], Tony Christian Landi [3], Oxana Drofa [3], Giorgio Veratti [3], Edoardo Fiorillo [4], Umberto Giostra [5] and Daiane de Vargas Brondani [1,6,*]

[1] CNR—Institute of Atmospheric Sciences and Climate, 73100 Lecce, Italy
[2] Department of Earth Sciences 'Ardito Desio', University of Milan, 20133 Milan, Italy; luca.mortarini@unimi.it
[3] CNR—Institute of Atmospheric Sciences and Climate, 40129 Bologna, Italy; tonychristian.landi@cnr.it (T.C.L.); o.drofa@isac.cnr.it (O.D.); g.veratti@isac.cnr.it (G.V.)
[4] CNR—Institute of Bioeconomy, 40129 Bologna, Italy; edoardo-fiorillo@cnr.it
[5] Department of Pure and Applied Sciences (DiSPeA), University of Urbino Carlo Bo, 61029 Urbino, Italy; umberto.giostra@uniurb.it
[6] Institute for Climate Change Solutions, 61029 Urbino, Italy
* Correspondence: daniela.cava@cnr.it (D.C.); daiane.devargasbrondani@uniurb.it (D.d.V.B.)

Abstract

Urban heat islands intensify heat stress and degrade air quality in densely built areas, yet the physical processes governing near-surface thermal variability remain poorly quantified. This study applies the coupled MOLOCH and PALM model system 6.0 (PALM-4U) over Bologna (Italy) during a summer 2023 heatwave to resolve meter-scale atmospheric dynamics within the Urban Canopy Layer and Roughness Sublayer at 2 m horizontal resolution. The coupled configuration was validated against in situ meteorological observations and Landsat-8 LST data, showing improved agreement in air temperature and wind speed compared to standalone mesoscale simulations. Results reveal pronounced diurnal and vertical variability of wind speed, turbulent kinetic energy, and friction velocity, with maxima between two/three times the median building height (h_c). Distinct surface-dependent contrasts emerge: asphalt and roofs act as strong daytime heat sources (Bowen ratio $\beta_{asphalt} \approx 4.8$) and nocturnal heat reservoirs at pedestrian level ($z \approx 0.07\ h_c$), while vegetation sustains daytime latent heat fluxes ($\beta_{vegetation} \approx 0.6 \div 0.8$) and cooler surface and near-surface air (Temperature anomaly of surface $\Delta T_s \approx -9\ ^\circ\mathrm{C}$ and air $\Delta T_{air} \approx -0.3\ ^\circ\mathrm{C}$). Thermal anomalies decay with height, vanishing above $z \approx 2.5\ h_c$ due to turbulent mixing. These findings provide insight into fine-scale energy exchanges driving intra-urban thermal heterogeneity and support climate-resilient urban design.

Keywords: urban heat island; PALM-4U; urban canopy layer; heatwave; microclimate; surface energy exchange; intra-urban thermal heterogeneity

check for updates

Received: 29 September 2025
Revised: 7 December 2025
Accepted: 9 December 2025
Published: 12 December 2025

Citation: Cava, D.; Mortarini, L.; Landi, T.C.; Drofa, O.; Veratti, G.; Fiorillo, E.; Giostra, U.; de Vargas Brondani, D. Energy Partitioning and Air Temperature Anomalies Above Urban Surfaces: A High-Resolution PALM-4U Study. *Atmosphere* **2025**, *16*, 1401. https://doi.org/10.3390/atmos16121401

1. Introduction

Cities are expanding rapidly worldwide and are increasingly recognized as drivers of major environmental and societal challenges, including resource depletion, air pollution, and the intensification of urban heat. Currently, about 54% of the global population resides in urban areas—a value expected to reach 66% by 2050, driven primarily by rapid urbanization in Asia and Africa [1]. This expansion, often occurring with limited planning, exacerbates thermal discomfort, air quality deterioration, and social vulnerability.

One of the most well-documented consequences of urbanization is the Urban Heat Island (UHI) effect, whereby cities exhibit higher air temperatures than their rural surroundings (typically 1–3 °C by day and up to 12 °C at night), with even larger contrasts in surface temperatures [2,3].

The UHI arises from the alteration of surface energy exchanges due to the replacement of natural vegetation with impervious materials such as asphalt, concrete, and rooftops. These materials absorb and retain heat because of their high thermal inertia while limiting latent heat fluxes through reduced evapotranspiration [4–7]. The resulting energy imbalance prolongs nocturnal heat retention, intensifying human heat exposure and health risks [8].

Urban energy partitioning—among radiative, sensible, latent, and storage fluxes—is strongly influenced by urban morphology, surface optical properties, and vegetation cover [9,10]. Reduced sky-view factor (SVF) in narrow canyons limits longwave cooling and sustains nighttime warming [11]. The three-dimensional geometry of buildings further modulates turbulence and air circulation within the Urban Canopy Layer (UCL)—the part of the atmosphere directly influenced by buildings and street canyons—and the overlying Roughness Sublayer (RSL), where flow and scalar fields remain affected by individual roughness elements. This interaction leads to pronounced spatial variability in energy fluxes and surface and near-surface temperature [12–16]. Thermal contrasts within cities can locally rival those observed between urban and rural areas, highlighting the need for high-resolution analyses capable of resolving pedestrian-scale processes [17,18].

Experimental studies in real cities remain limited due to the logistical challenges and cost of dense measurement networks [16,19]. Consequently, numerical modeling—particularly Large-Eddy Simulation (LES)—has become a key tool for resolving the turbulent exchanges that control urban microclimates [20–22]. LES explicitly resolves the unsteady three-dimensional dynamics of flow, turbulence, and scalar transport within realistic city geometries.

This study builds on ongoing work within the author's group, which developed and is currently validating a coupled MOLOCH–PALM-4U modeling system [23] over the city of Bologna during a severe heatwave in August 2023. MOLOCH4PALM is a new interface that provides dynamic boundary conditions for PALM-4U [24] using mesoscale fields generated by the MOLOCH model [25]. In this work, the performance of the coupled system is assessed through two complementary comparisons: modeled near-surface meteorological fields against in situ observations, and modeled surface temperature against satellite-derived Land Surface Temperature (LST) from the Landsat-8 overpass during the same period. These evaluations show that the coupled MOLOCH–PALM-4U system reproduces both atmospheric conditions and surface temperature patterns with satisfactory accuracy, supporting its reliability for analyzing urban energy fluxes and intra-urban thermal variability.

Building on this validated framework, the present study investigates fine-scale energy exchange and thermal variability within the Bolognina district during the August 2023 heatwave. The study specifically aims to (i) Quantify the diurnal and vertical variability of wind speed (U), turbulent kinetic energy (TKE), and friction velocity (u_*) within the UCL and RSL at 2 m resolution; (ii) Compare sensible and latent heat fluxes (H, LE) and Bowen ratios (β) across major urban surface types (asphalt, concrete, vegetation, roofs); and (iii) Characterize the air-temperature anomalies (ΔT_{air}) and their attenuation with height, linking them to surface heterogeneity and local energy balance.

By applying meter-scale LES to a real European district with detailed urban morphology and event-specific mesoscale forcing, this study provides an insightful analysis of the processes driving intra-urban thermal heterogeneity and offers guidance for effective urban heat mitigation strategies.

2. MOLOCH and PALM-4U Coupling and Case Study Overview

This study employs a coupled modeling system that integrates the mesoscale non-hydrostatic MOLOCH model [25] with the microscale model PALM-4U (version 6.0; [24]) through the novel offline nesting interface MOLOCH4PALM [23]. The coupling procedure allows the simulation of urban meteorology at meter-scale resolution by incorporating three-dimensional, time-varying meteorological fields from MOLOCH into PALM-4U. Details on model configuration and boundary forcing are provided in Section 2.1.

The modeling system was tested over the city of Bologna (Italy) during an extreme heatwave in August 2023. The study area corresponds to the Bolognina district, located north of Bologna's historic center, characterized by high urban density and mixed residential, commercial, and industrial zones. Simulations were performed using a three-domain nesting approach, all centered on the study area (44°30′43″ N, 11°20′47″ E; Figure 1).

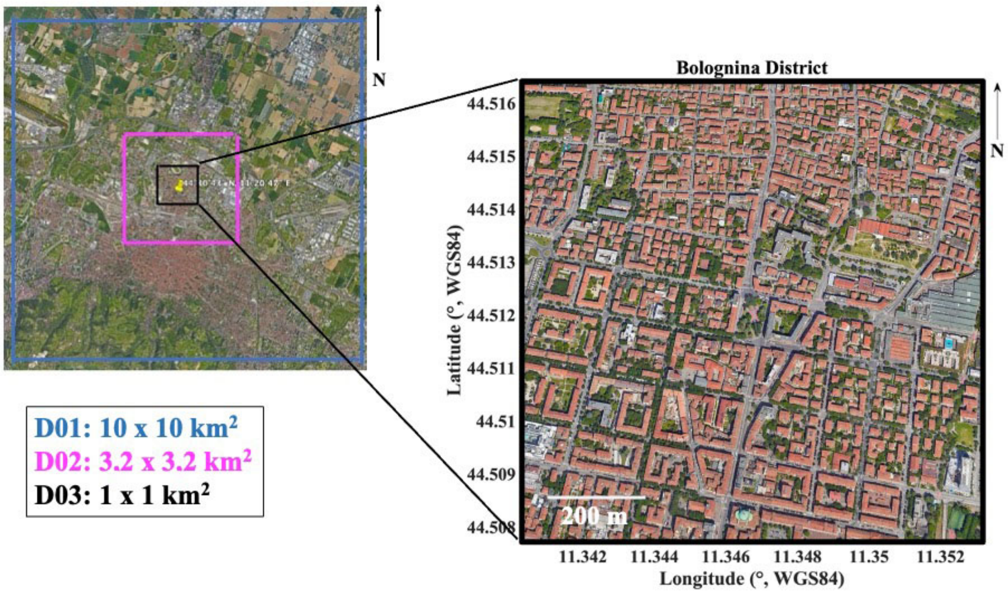

Figure 1. Nested modeling domains used in the MOLOCH–PALM-4U setup. D01 (outer domain, 50 m isotropic grid spacing; 10 km × 10 km horizontal extent; 3 km vertical extent), D02 (intermediate domain, 10 m isotropic grid spacing; 3.2 km × 3.2 km horizontal extent; 1.6 km vertical extent), and D03 (innermost domain, 2 m isotropic grid spacing; 1 km × 1 km horizontal extent; 280 m vertical extent) are shown, with the inset highlighting the Bolognina district represented in D03. Background satellite imagery from Google Earth (Imagery © Google Earth) is included for spatial context. The inset is shown in geographic coordinates (°E, °N; WGS84) with a north arrow and a 200 m scale bar.

The coarsest domain D01 covers an area of 10 km × 10 km with a uniform horizontal and vertical grid spacing of 50 m, extending up to 3 km above ground level. The intermediate domain D02 has a horizontal and vertical resolution of 10 m and an extent of 3.2 km × 3.2 km, reaching a height of approximately 1.6 km. The innermost domain D03 corresponds to the Bolognina district, covering a 1 km^2 urban area with 2 m isotropic grid spacing and a model top at about 280 m.

In this study, the GEO4PALM tool [26] was used to generate the static drivers for domains D01 and D02, whereas an ad hoc workflow based on the rPALM library [27] was developed for D03. For D01 and D02, ESA WorldCover classes were converted into PALM-4U categories (vegetation, pavement, building, water, soil), and street morphology was obtained from OpenStreetMap. The D03 static driver was produced from high-resolution geospatial data compiled from multiple sources. Most datasets were downloaded from the Bologna Municipal Geoportal, while other layers—such as private tree information—were created through field surveys and photo-interpretation of high-resolution imagery.

A dedicated *R* procedure was implemented to integrate these datasets, compute required variables (e.g., leaf area density, surface fractions), and to assemble the final static driver using rPALM. Terrain elevation (with 5 m resolution) was obtained from the Emilia-Romagna Geoportal. Building-related variables (building_type, building_id, building_2d) was derived from municipal vector layers. The vegetation_type layer was produced using: (i) a complete inventory of public and private trees [28], (ii) field mapping of private trees conducted in 2023, and (iii) photo-interpretation for short-grass areas. Private tree data were collected with a customized QField app, recording biometric traits required for LAD computation; species identification was supported by experts and the PlantNet app. LAD for individual trees was calculated using the f.calc_single_tree function of rPALM [29]. The pavement_type layer was derived through field surveys and imagery interpretation, while street_type originated from OpenStreetMap, which provides five categories of one-way and two-way roads relevant for the D03 domain.

Land cover classification for the Bolognina district (Figure 2) reveals that impervious surfaces dominate, with asphalt (38.8%) and roofs (33.3%) accounting for over 70% of the total area, while vegetated surfaces are comparatively limited (grass: 4.8%; trees: 8.1%). The vertical leaf area density (LAD) profile (Figure 3a) shows that most vegetation is confined below 10 m, with a peak between 4 and 6 m corresponding to street trees and a smaller peak above 15 m from taller canopies. This vertical structure suggests a discontinuous yet stratified urban green cover within the district. Building heights in D03 range from about 1 m to over 30 m, with a median height of 14.5 m and an interquartile range of 9–18 m, pointing to a predominantly homogeneous building stock with a few significantly taller structures (Figure 3b). The relative scarcity of vegetation above building height indicates limited canopy overlap with rooftops, implying that most green cover interacts primarily with the pedestrian and street level. The median value of buildings is adopted in this study as the reference 'average canopy height' (h_c = 14.5 m) for the normalization of vertical profiles and dimensionless scaling of turbulence quantities.

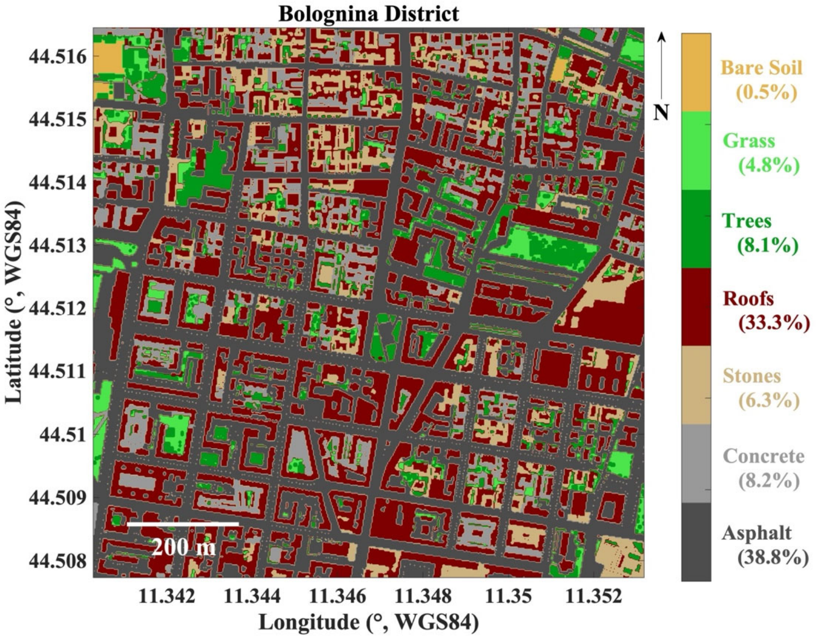

Figure 2. Land-cover classification for domain D03 (Bolognina District), showing the spatial distribution of the major surface types: bare soil (1261 grid cells; 0.5%), grass (11,809; 4.8%), trees (20,214; 8.1%), roofs (83,250; 33.3%), stones (15,850; 6.3%), concrete (20,499; 8.2%), and asphalt (97,117; 38.8%). The panel is displayed in geographic coordinates (°E, °N; WGS84) with a north arrow and a 200 m scale bar.

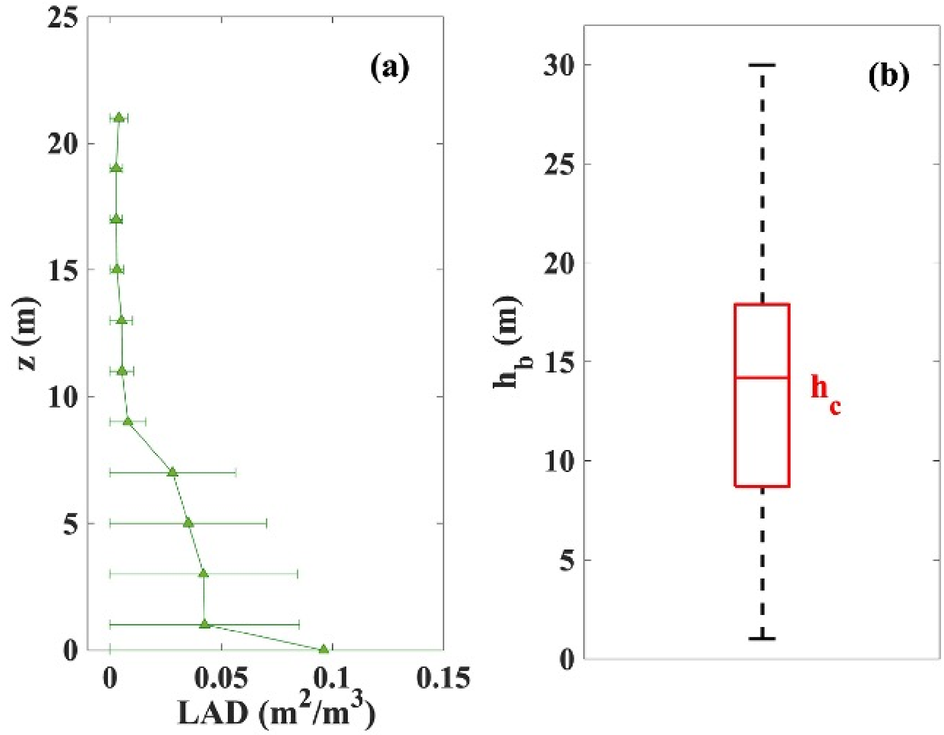

Figure 3. (**a**) Vertical profile of mean leaf area density (LAD) for all vegetated grid cells in D03. Dots indicate the layer-mean LAD, and bars denote the standard deviation across grid cells at each height. (**b**) Building-height distribution within D03 shown as a boxplot. The median canopy height is 14.5 m, with an interquartile range of 9–18 m and individual outliers spanning 1–30 m.

The simulation spans 23–25 August 2023, characterized by clear skies, intense solar radiation, and weak winds, typical of summer urban heat island conditions. To minimize boundary-induced transients, the first 24 h were discarded as spin-up as recommended by [24] to equilibrate soil, wall, and pavement temperatures at initialization. Analyses focus on 24–25 August, covering two full diurnal cycles under quasi-stationary meteorological conditions.

2.1. Model Configuration and Forcing

Building upon the coupling framework introduced in Section 2, this section details the specific configuration of the PALM-4U domains and the procedure used to ingest mesoscale meteorological forcings from MOLOCH through the MOLOCH4PALM interface. We describe the treatment of initial and boundary conditions, grid setup, radiative and thermal parameterization, and the rationale for the selected spin-up strategy.

MOLOCH4PALM, an adaptation of the INIFOR tool originally developed for COSMO–PALM coupling [30], converts the hourly 3-D meteorological MOLOCH fields into initial and time-dependent boundary conditions for PALM-4U. The tool interpolates MOLOCH wind components, temperature, humidity, pressure and radiative fields onto the PALM grid following the fixed PALM dynamic-driver structure. Horizontal interpolation is bilinear, while vertical interpolation follows PALM's driver requirements. The upper and lateral boundaries of PALM-4U are forced with these temporally interpolated fields (linear interpolation between hourly MOLOCH outputs). No additional large-scale nudging was applied within the PALM domain. The Synthetic Turbulence Generator (STG) built into PALM-4U [31] was activated through MOLOCH4PALM to inject turbulent fluctuations at the boundaries, compensating for the absence of resolved turbulence in MOLOCH and ensuring a physically consistent turbulence spin-up at meter-scale resolution. MOLOCH4PALM is openly available (https://git.isac.cnr.it/landi/moloch4palm (accessed on 6 December 2025)) [23].

Three nested PALM-4U domains (D01, D02, D03) were used, with uniform (non-stretched) grid spacing in all directions. This choice was driven by (i) the nesting requirements of PALM version 23.10 and (ii) the need to preserve vertical resolution for boundary-layer dynamics in D02 (10 m spacing) and for surface–atmosphere heat exchange in D03 (2 m spacing).

The outer domain (D01, 50 m) was defined substantially larger than the validation area to ensure a sufficiently wide relaxation zone and smooth transition from the 1.25 km MOLOCH fields to mesoscale-LES scales. No large-scale nudging was applied, and mesoscale fields were linearly interpolated in time between the hourly MOLOCH outputs according to the default MOLOCH4PALM driver settings.

PALM-4U employs a 1.5-order TKE closure, a 5th-order upwind-biased advection scheme, and a 3rd-order Runge–Kutta time integration. The perturbation pressure equation is solved using a multigrid solver with FFTW. Energy-balance modules for buildings and pavements are activated, and no-slip Dirichlet conditions are applied to horizontal velocity components and subgrid-scale TKE at solid surfaces. Radiative transfer was handled by the Rapid Radiative Transfer Model for Global Models (RRTMG).

Radiative and thermal properties (albedo, emissivity, heat capacity and thermal conductivity for impervious materials; stomatal and vegetation parameters for trees, grass and shrubs) were taken from the default PALM-4U material and vegetation libraries. Roofs were represented using the standard PALM-4U single-layer substrate scheme, which treats the roof as a homogeneous slab with prescribed thermal conductivity, heat capacity, and thickness. This simplified parameterization includes a single prognostic substrate temperature and does not account for multi-layer internal heat storage. Since no site-specific measurements were available, all parameters were used exactly as specified in the official PALM technical documentation (https://palm.muk.uni-hannover.de/trac/wiki/doc/app/radiation_parameters (accessed on 28 September 2025)).

A 24 h spin-up was applied prior to the 48 h analysis period (24–25 August 2023). This duration follows the recommendations of [24] for urban LES with coupled land-surface modules. PALM initializes longwave and shortwave radiative fluxes using precomputed lookup tables (LUTs), and soil/wall/roof temperatures using its default land-surface routines.

All time references in figures and analysis correspond to Local Standard Time (LT), which for Bologna equals Central European Time (CET, UTC + 1 h). This convention was adopted to ensure consistency and reproducibility across simulations and observations. Note that the abbreviation LT is used to avoid confusion with Land Surface Temperature (LST).

2.2. Validation and Uncertainty

To evaluate the ability of the coupled MOLOCH–PALM-4U system to reproduce near-surface thermal dynamics during the heatwave, simulated 2 m air temperatures were compared against in situ observations from two CNR-ISAC stations and ten Weather Underground sites (www.wunderground.com (accessed on 28 September 2025)). Figure 4 presents conditional quantile plots of observed versus modeled temperatures, complemented by summary statistics. The agreement for the MOLOCH–PALM-4U system (Figure 4b) is generally strong, with a coefficient of determination R^2 = 0.72 and a regression slope of 1.07, indicating that the model captures the diurnal thermal cycle and variability across regimes. The overall RMSE is 2.61 °C, while the mean bias is -0.56 °C, confirming a slight warm bias of the model. Relative error metrics remain moderate (MAPE $\approx$ 6.9%, sMAPE ≈ 7.0%), and the normalized mean bias (NMBE) is below 2%, suggesting that systematic deviations are small compared to the observed range. Conditional quantile envelopes reveal that PALM-4U reproduces high-temperature conditions more accurately than MOLOCH alone (Figure 4a), reducing the cold bias typically associated with coarse urban-canopy representation. While MOLOCH underestimates daily maxima by about 3.5 °C, PALM-4U substantially mitigates this cold bias and better resolves extreme heat conditions, owing to its explicit representation of urban geometry and surface energy exchange. These results demonstrate that the coupled system retains large-scale synoptic forcing while realistically downscaling thermal variability at the urban canopy scale. The combination of high correlation, low bias, and moderate RMSE provides confidence in the model's ability to support microclimate analyses and heat-mitigation strategies.

To further assess the realism of simulated surface temperatures, PALM-4U results were compared in this work with Landsat-8 Land Surface Temperature (LST) data acquired over Bologna on 23 August 2023 at 10:00 LT. The satellite overpass occurred one day before the simulated period (24–25 August), under comparable clear-sky and weak-wind conditions, allowing for a quasi-stationary comparison.

Figure 5 compares the simulated surface temperature field (T_S) from PALM-4U at 10:00 LT on 24 August 2023 (Figure 5b) with the Landsat-derived LST acquired one day earlier (23 August 2023) (Figure 5a). Model output was spatially upscaled ($T_{S(up)}$) to the 30 m Landsat pixel resolution by averaging all grid cells within each satellite footprint, thereby minimizing the scale mismatch between the two datasets (Figure 5c). The two fields exhibit a broadly consistent spatial structure. Although absolute magnitudes differ locally, the model reproduces the main temperature pattern across the domain. The highest surface temperatures predicted by PALM-4U occur over rooftops and asphalt surfaces, with maxima around 55–60 °C. These hotspots correspond to elevated regions in the Landsat image, albeit with a slightly lower intensity; deviations at the warmest points remain within ~10 °C which is reasonable given the inherent physical differences between the modeled ground temperature and the satellite-retrieved radiometric temperature, as well as their distinct spatial scales. In contrast, cooler areas related to vegetation or shaded streets are less distinctly represented in the satellite field, likely due to its coarser spatial resolution and radiometric averaging of mixed land-cover types within each pixel. Figure 5d illustrates the spatial pattern of $\Delta T = T_{S(up)} - \text{LST}$. Differences exhibit a marked spatial variability, with the largest deviations occurring in shaded areas or in zones characterized by complex surface morphology. The probability distributions of ΔT for the two analyzed days (Figure 6) are well approximated by a normal distribution, with the peak shifted slightly toward negative values, indicating a modest systematic cold bias. Gaussian fits yield mean and standard-deviation values of $\mu = -4.0$ °C, $\sigma = 4.8$ °C for 24 August, and $\mu = -2.7$ °C, $\sigma = 4.1$ °C for 25 August. The Kolmogorov–Smirnov test applied to the normalized residuals gives $p = 0.37$ and 0.41 for the two days, indicating no significant departure from normality at the 5% level. These results confirm that discrepancies between modeled and satellite LST behave largely as random, scale-dependent fluctuations around a small systematic bias, consistent with the one- to two-day temporal offset between the two datasets and with their different spatial resolutions.

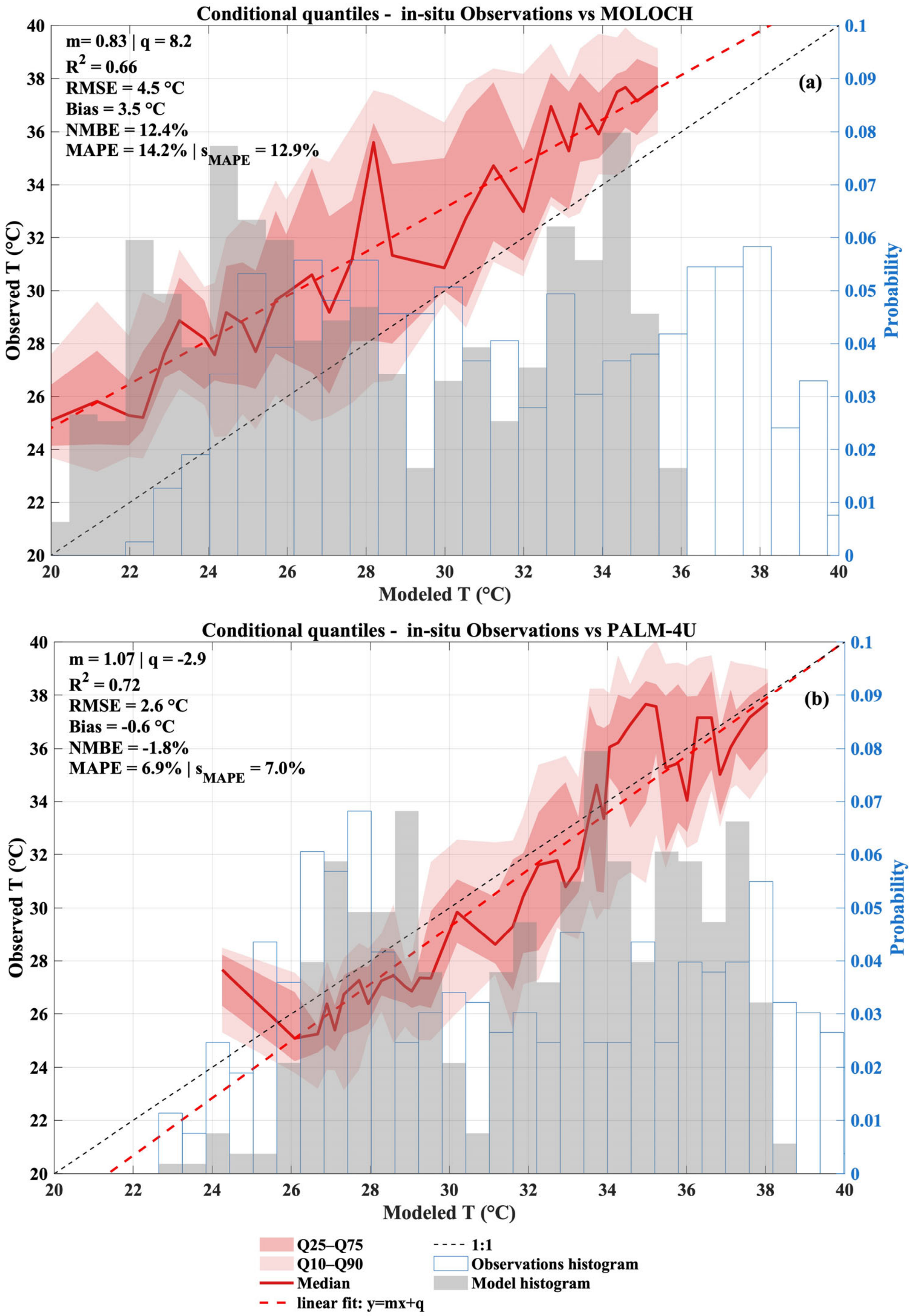

Figure 4. Conditional quantile comparison of observed vs. simulated 2 m air temperatures with MOLOCH (**a**) and MOLOCH-PALM-4U (**b**). Shaded envelopes indicate interquartile ranges (Q25–Q75) and decile ranges (Q10–Q90); continuous red lines indicate median values; dashed red and black lines mark the linear fit and perfect agreement (1:1), respectively. The gray and blue bars are normalized histograms showing the distribution of modeled and observed temperatures, respectively, on the blue secondary axis (probability), providing context on how values are spread across the range.

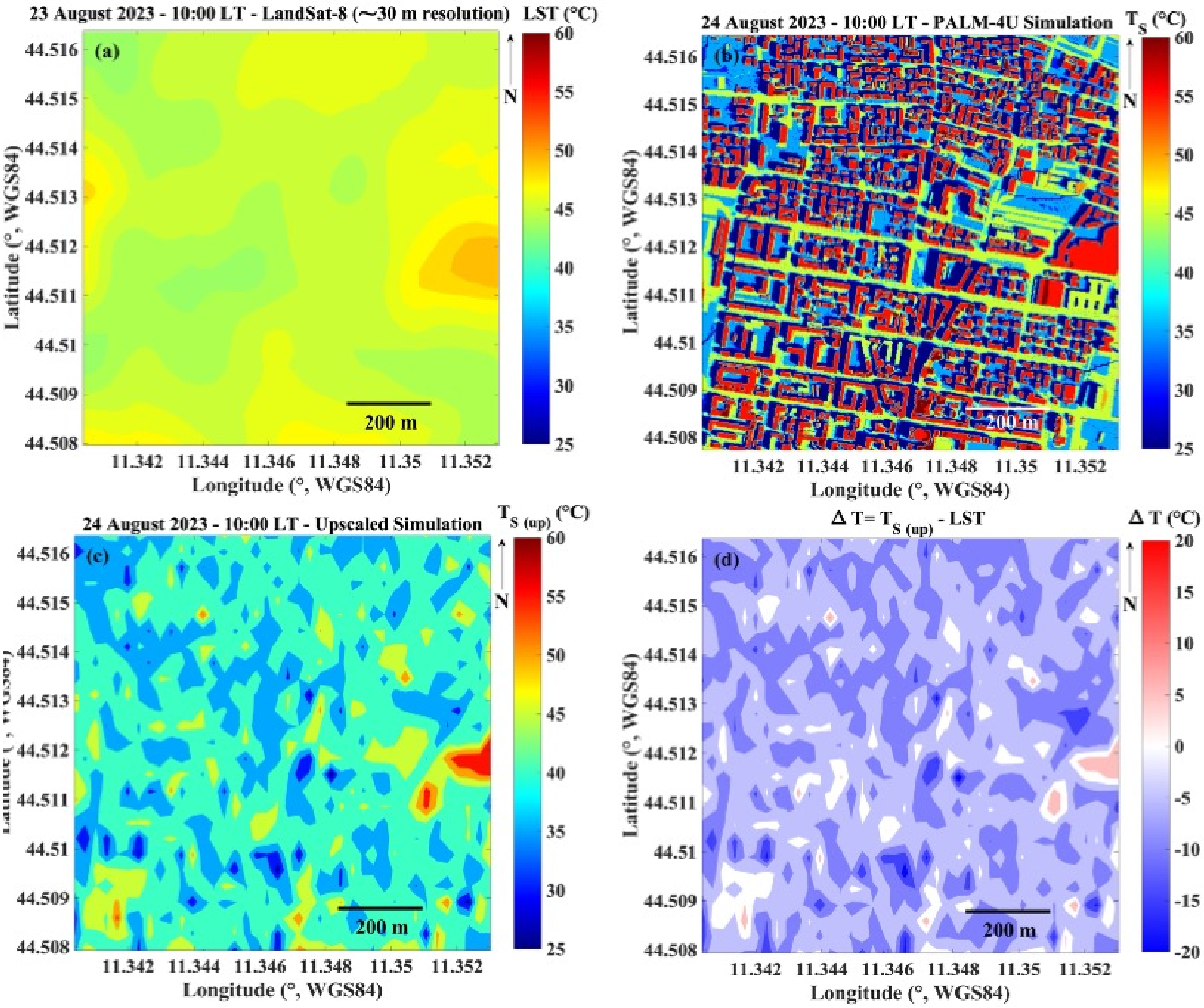

Figure 5. Comparison between simulated and satellite-derived surface temperatures over the Bolognina district (Bologna, Italy): (**a**) Land Surface Temperature (LST) retrieved from Landsat-8 on 23 August 2023 at 10:00 LT (30 m resolution); (**b**) PALM-4U simulated surface temperature (T_s) on 24 August 2023 at 10:00 LT (2 m resolution); (**c**) Simulated T_s upscaled to 30 m to match the Landsat spatial resolution ($T_{S(up)}$); (**d**) Temperature difference field ($\Delta T = T_{S(up)} - \text{LST}$) highlighting local warm and cool deviations between model and satellite estimates. Time is LT (Local Standard Time, CET = UTC + 1 h). All panels are shown in geographic coordinates (°E, °N, WGS84) with north arrow and a 200 m scale bar. Color bars report absolute temperature (°C) or temperature anomaly (°C) as indicated.

The Q–Q analysis (Figure 7) shows that PALM-4U reproduces the general T_S distribution but exhibits larger variability compared to LST. Model quantiles extend beyond those of the satellite data, reflecting the model's ability to resolve fine-scale thermal contrasts such as sunlit walls and roofs. The relatively low correlation coefficient (R $\approx$ 0.28–0.29) primarily reflects the intrinsic differences between satellite-derived radiometric land surface temperature and modeled kinetic radiative-skin temperature. Landsat LST retrievals rely on emissivity assumptions that may not fully match the material parameters prescribed in PALM-4U, especially for heterogeneous urban surfaces such as mixed roofing and façade–street pixels [32–34]. In addition, the fixed off-nadir viewing angle of Landsat (~9–11°) samples a composite signal from rooftops, asphalt, and shaded walls, whereas PALM-4U explicitly resolves the full 3D urban geometry and computes face-specific temperatures, distinguishing sunlit and shaded elements [35–37]. Shadowing effects are therefore represented differently: PALM accounts for radiative obstruction and reduced shortwave input, while Landsat partially integrates diffuse radiance contributions that attenuate apparent thermal contrast [35,37]. These structural and methodological mismatches naturally reduce spatial correlation, even when the physical surface temperatures are realistically reproduced by the model. Despite these limitations, the comparison confirms that the coupled MOLOCH–PALM-4U system captures the spatial organization and intensity of surface heating over the urban core, supporting its use as a physically consistent tool for urban climate analysis.

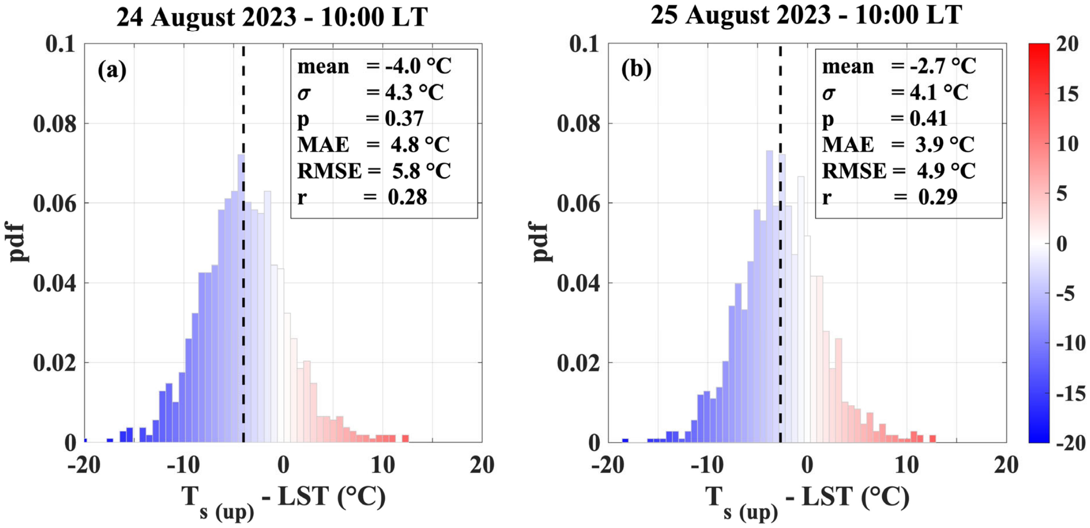

Figure 6. Probability density function (pdf) of the difference between simulated surface temperature (T_s) from PALM-4U and satellite-derived Land Surface Temperature (LST) from Landsat-8 for (**a**) 24 and (**b**) 25 August 2023 (10:00 LT). Gaussian fits yield $\mu \approx -4.0$ and -2.7 °C, $\sigma \approx 4.3$ and 4.1 °C, respectively, and $p > 0.05$ (Kolmogorov–Smirnov) for both days, confirming near-normal behavior and a modest systematic cold bias. Time is LT (Local Standard Time, CET = UTC + 1 h).

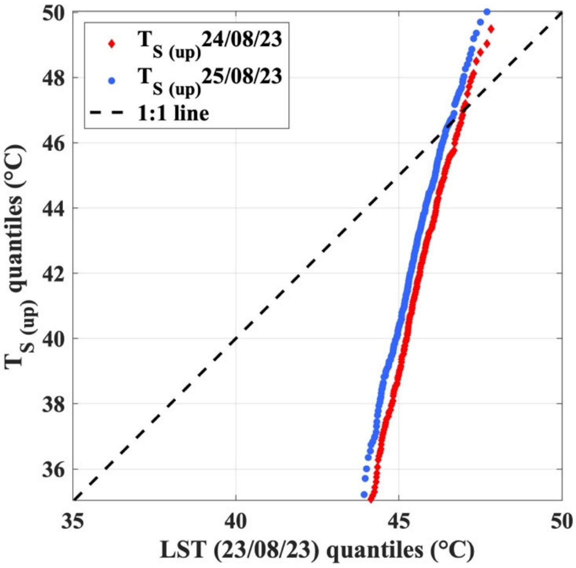

Figure 7. Quantile–Quantile (Q–Q) plot of modeled surface temperature quantiles (T_s) for 24 August (red diamonds) and 25 August 2023 (blue circles) at 10:00 LT, versus Landsat-derived Land Surface Temperature (LST) from the 23 August 2023 overpass at 10:00 LT. The dashed line is the 1:1 reference. Time is LT (Local Standard Time, CET = UTC + 1 h).

These results strongly suggest that integrating mesoscale and microscale components is crucial for accurately simulating local meteorological fields within the urban canopy. This integrated approach provides confidence in the model's ability to analyze energy fluxes and intra-urban thermal variability.

3. Results

The high-resolution PALM-4U simulations provide a detailed characterization of the turbulent, thermal and moisture fields in the Bolognina district under extreme summer conditions. The following subsections present: (i) the vertical and temporal structure of dynamical and thermodynamic variables, (ii) the diurnal cycles of surface energy fluxes and temperatures, and (iii) the microclimatic imprint of different land covers on air temperature in the UCL and RSL.

3.1. Dynamical and Thermal Flow Characteristics in the Urban Canopy and Roughness Sublayers

In this section, the dynamical and thermal characteristics of the flow within the Urban RSL and the UCL, across a variety of impervious and vegetated surfaces and under contrasting daytime and nighttime conditions, have been explored. Figure 8 shows the temporal evolution of vertical profiles of averaged wind speed (U), turbulent kinetic energy (TKE), and friction velocity (u_*). All quantities represent domain-mean values at each height and time step, averaged over the entire innermost PALM-4U domain (D03) to capture the overall vertical and temporal evolution of the urban boundary layer. Distinct diurnal patterns emerge, with enhanced turbulence during the daytime, consistent with buoyancy-driven mixing commonly observed in urban environments under strong solar forcing.

To complement this domain-integrated overview, Figure 9 presents nocturnal (left panels) and diurnal (right panels) vertical profiles of normalized wind speed ($U/\overline{U_{hc}}$), vertical velocity standard deviation ($\sigma_w/\overline{U_{hc}}$), and squared friction velocity ($u_*/\overline{u_{*hc}})^2$, separately computed for asphalt, concrete, paving stones, rooftops, bare soil, grass, and tree-covered areas. For the vertical profiles, the normalization is based on the median building height (h_c = 14.5 m), used as a representative canopy reference for the study area. Within each surface class, statistics are computed by selecting all grid points in D03 associated with that surface type and averaging them over the defined daytime (10:00–18:00 LT) and nighttime (23:00–05:00 LT) periods. Each variable is then normalized using the corresponding domain-averaged value at canopy height, calculated over the same time window. This normalization (denoted by overbars) highlights departures from the domain-mean behavior and isolates the specific contribution of each surface type. Daytime (10:00–18:00 LT) and nighttime (23:00–05:00 LT) periods were selected to represent typical convective and stable regimes under clear-sky conditions. These intervals correspond to hours characterized by quasi-stationary radiative forcing and well-developed turbulent structures, as confirmed by the diurnal evolution of fluxes and turbulence statistics. Transitional hours near sunrise and sunset were excluded to minimize non-stationary effects associated with rapidly changing stability. The resulting averages should therefore be interpreted as representative of typical daytime and nocturnal conditions rather than as strictly stationary states. For the key variables, mean values together with their standard deviations are reported to quantify variability across both diurnal regimes and surface types (Tables 1 and 2).

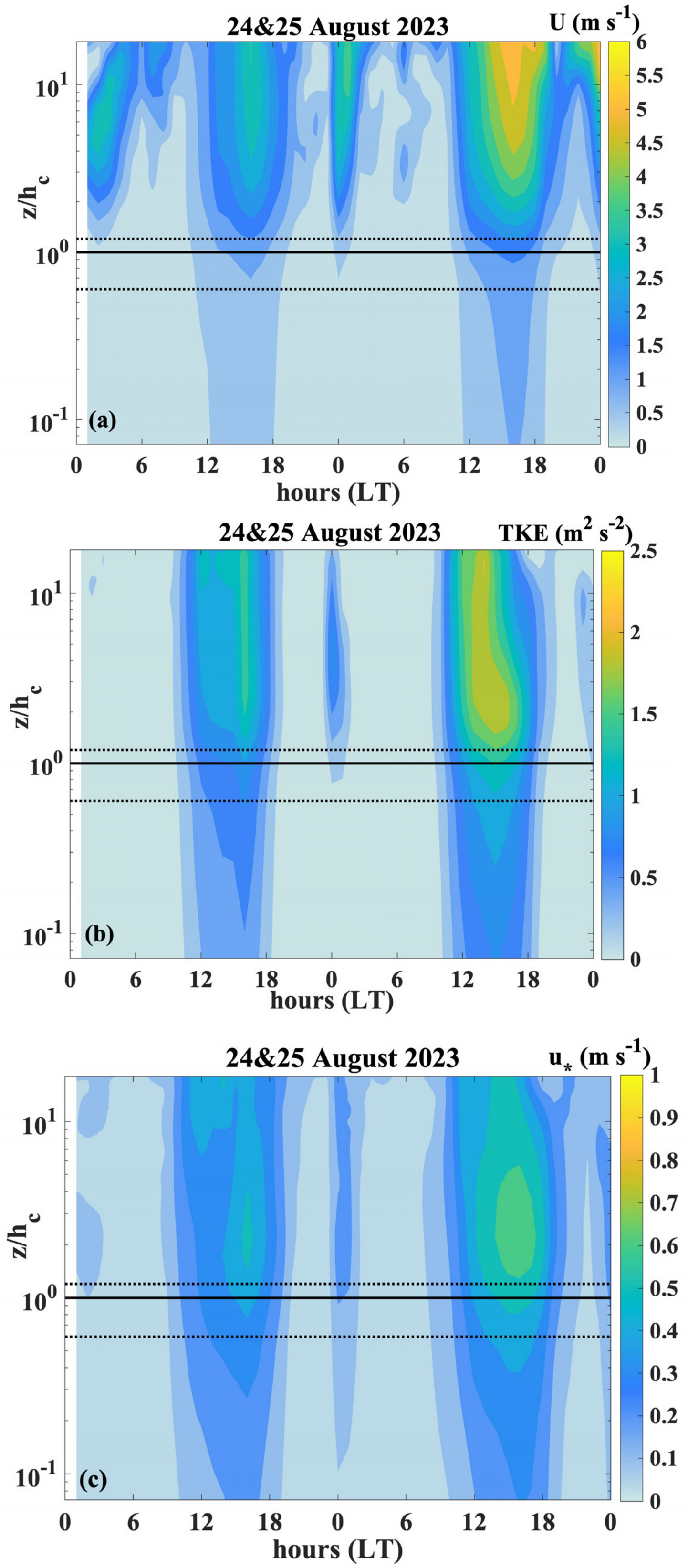

Figure 8. Temporal evolution of domain-averaged (**a**) wind speed *U* (m s^{-1}), (**b**) turbulent kinetic energy *TKE* (m^2 s^{-2}), and (**c**) friction velocity u_* (m s^{-1}) in the Bolognina district from 24 to 25 August 2023. Values are averaged over the innermost domain (D03) and shown as a function of normalized height (z/h_c) and LT. Horizontal continuous and dotted lines mark, respectively, the median (14.5 m) and interquartile range (9–18 m) of the building height distribution. Time is LT (Local Standard Time, CET = UTC + 1 h).

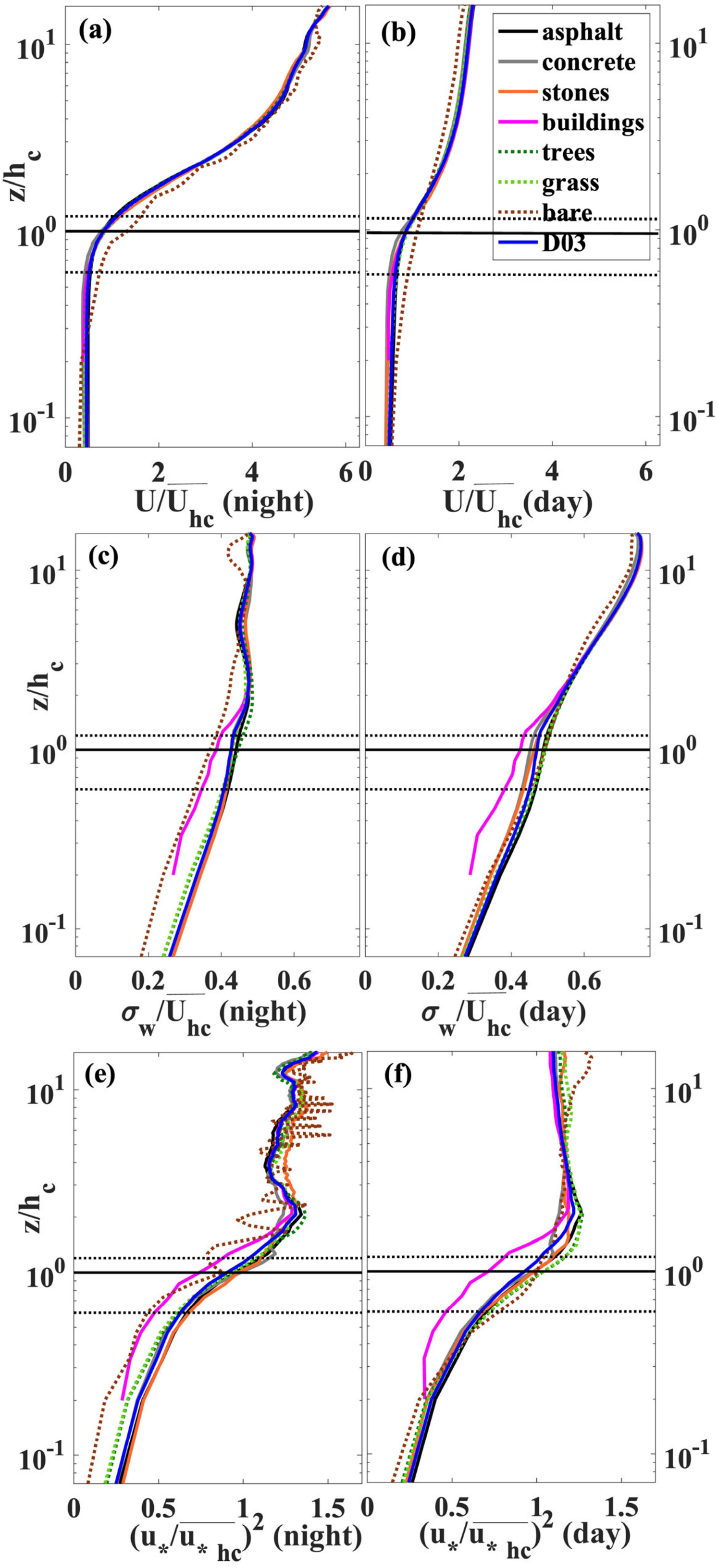

Figure 9. Nocturnal (**left panels**) and diurnal (**right panels**) average vertical profiles of (**a**,**b**) normalized mean wind speed, (**c**,**d**) normalized vertical velocity standard deviation, and (**e**,**f**) normalized squared friction velocity over different surface types in the Bolognina district. Normalization is performed with respect to the domain-averaged statistics at canopy height computed for the D03 innermost domain (indicated by the overbars). Solid black lines show the median building height (14.5 m), and dotted lines indicate the interquartile range (9–18 m) of the building height distribution.

Table 1. Mean ± standard deviation of turbulent variables—horizontal wind speed (U), vertical velocity standard deviation (σ_w), friction velocity (u*), and turbulent kinetic energy (*TKE*)—for the full D03 domain and each surface class. Statistics are shown at three heights (pedestrian level, z/hc = 1, and z/hc = 2) and for daytime (10:00–18:00 LT) and nighttime (23:00–05:00 LT) periods. Values represent averages over all grid points of the corresponding surface type at the specified height.

Surface Type	*z/hc*	Period	U (m s^{-1})	σ_w (m s^{-1})	u_* (m s^{-1})	*TKE* (m^2 s^{-2})
D03	0.07	Day	0.65 ± 0.24	0.35 ± 0.23	0.20 ± 0.06	0.50 ± 0.21
		Night	0.16 ± 0.09	0.09 ± 0.09	0.05 ± 0.03	0.04 ± 0.04
Asphalt	0.07	Day	0.68 ± 0.25	0.35 ± 0.23	0.21 ± 0.07	0.52 ± 0.22
		Night	0.17 ± 0.09	0.09 ± 0.09	0.05 ± 0.03	0.04 ± 0.04
Concrete	0.07	Day	0.57 ± 0.18	0.33 ± 0.22	0.20 ± 0.06	0.40 ± 0.17
		Night	0.15 ± 0.06	0.09 ± 0.09	0.05 ± 0.02	0.03 ± 0.03
Stones	0.07	Day	0.57 ± 0.20	0.33 ± 0.22	0.20 ± 0.06	0.43 ± 0.18
		Night	0.17 ± 0.07	0.09 ± 0.09	0.05 ± 0.02	0.03 ± 0.03
Buildings	0.07	Day	---	---	---	---
		Night	---	---	---	---
Trees	0.07	Day	0.63 ± 0.22	0.34 ± 0.22	0.18 ± 0.06	0.50 ± 0.20
		Night	0.15 ± 0.09	0.08 ± 0.07	0.04 ± 0.02	0.04 ± 0.04
Grass	0.07	Day	0.64 ± 0.23	0.34 ± 0.22	0.20 ± 0.06	0.54 ± 0.23
		Night	0.15 ± 0.09	0.08 ± 0.07	0.04 ± 0.02	0.04 ± 0.04
Bare	0.07	Day	0.72 ± 0.26	0.31 ± 0.19	0.16 ± 0.04	0.62 ± 0.25
		Night	0.11 ± 0.07	0.07 ± 0.05	0.03 ± 0.02	0.03 ± 0.03
D03	1	Day	1.13 ± 0.46	0.60 ± 0.38	0.40 ± 0.12	0.90 ± 0.39
		Night	0.29 ± 0.24	0.15 ± 0.14	0.09 ± 0.06	0.08 ± 0.07
Asphalt	1	Day	1.13 ± 0.46	0.63 ± 0.39	0.41 ± 0.12	0.90 ± 0.38
		Night	0.28 ± 0.24	0.16 ± 0.16	0.10 ± 0.06	0.08 ± 0.07
Concrete	1	Day	1.01 ± 0.40	0.58 ± 0.37	0.41 ± 0.12	0.82 ± 0.36
		Night	0.27 ± 0.23	0.15 ± 0.13	0.10 ± 0.07	0.07 ± 0.06
Stones	1	Day	1.12 ± 0.43	0.59 ± 0.37	0.41 ± 0.12	0.89 ± 0.38
		Night	0.30 ± 0.25	0.15 ± 0.15	0.10 ± 0.06	0.08 ± 0.07
Buildings	1	Day	1.14 ± 0.47	0.55 ± 0.35	0.35 ± 0.10	0.91 ± 0.39
		Night	0.30 ± 0.25	0.14 ± 0.12	0.09 ± 0.05	0.08 ± 0.06
Trees	1	Day	1.16 ± 0.47	0.63 ± 0.39	0.42 ± 0.13	0.95 ± 0.40
		Night	0.29 ± 0.25	0.16 ± 0.16	0.10 ± 0.07	0.08 ± 0.07
Grass	1	Day	1.13 ± 0.49	0.60 ± 0.38	0.42 ± 0.13	0.96 ± 0.41
		Night	0.30 ± 0.26	0.15 ± 0.14	0.10 ± 0.07	0.08 ± 0.07
Bare	1	Day	1.43 ± 0.56	0.63 ± 0.38	0.41 ± 0.12	1.02 ± 0.43
		Night	0.47 ± 0.45	0.13 ± 0.12	0.09 ± 0.07	0.09 ± 0.07
D03	2	Day	1.96 ± 0.96	0.68 ± 0.39	0.45 ± 0.15	1.22 ± 0.52
		Night	0.83 ± 0.61	0.17 ± 0.16	0.11 ± 0.08	0.15 ± 0.14
Asphalt	2	Day	1.96 ± 0.98	0.69 ± 0.40	0.46 ± 0.15	1.23 ± 0.53
		Night	0.82 ± 0.60	0.17 ± 0.16	0.11 ± 0.08	0.15 ± 0.14

Table 1. *Cont.*

Surface Type	z/hc	Period	U (m s^{-1})	σ_w (m s^{-1})	u_* (m s^{-1})	TKE (m^2 s^{-2})
Concrete	2	Day	1.96 ± 0.92	0.67 ± 0.39	0.44 ± 0.15	1.19 ± 0.50
		Night	0.85 ± 0.64	0.17 ± 0.15	0.11 ± 0.08	0.15 ± 0.13
Stones	2	Day	2.03 ± 0.95	0.68 ± 0.37	0.45 ± 0.15	1.20 ± 0.52
		Night	0.85 ± 0.63	0.17 ± 0.16	0.11 ± 0.08	0.15 ± 0.13
Buildings	2	Day	1.97 ± 0.97	0.67 ± 0.38	0.44 ± 0.15	1.22 ± 0.53
		Night	0.83 ± 0.61	0.17 ± 0.15	0.11 ± 0.08	0.15 ± 0.12
Trees	2	Day	1.93 ± 0.93	0.69 ± 0.40	0.47 ± 0.15	1.21 ± 0.52
		Night	0.82 ± 0.61	0.17 ± 0.17	0.12 ± 0.08	0.15 ± 0.14
Grass	2	Day	1.96 ± 0.96	0.69 ± 0.40	0.46 ± 0.16	1.22 ± 0.52
		Night	0.83 ± 0.61	0.17 ± 0.16	0.11 ± 0.08	0.15 ± 0.14
Bare	2	Day	1.84 ± 0.70	0.69 ± 0.40	0.44 ± 0.16	1.13 ± 0.46
		Night	0.95 ± 0.78	0.15 ± 0.15	0.10 ± 0.06	0.13 ± 0.12

Within the UCL, wind speed remains generally low near pedestrian level, with nocturnal values typically below 0.5 m s^{-1} and daytime maxima rarely exceeding 1–1.5 m s^{-1} (Figure 8a). This reflects the strong drag and momentum absorption associated with the dense and heterogeneous urban morphology [13]. In the RSL, wind speed increases sharply above the canopy top, with a clear inflection near $z \approx h_c$, more pronounced at night (Figure 8a), in agreement with documented behavior of flows above vegetated and urban canopies [14,22,38–43]. Above this transition, enhanced vertical shear drives turbulence production, generating local maxima of TKE and $u*$ between ≈2–3 h_c (Figure 8b,c). These peaks are more evident during the afternoon, when buoyancy reinforces mechanical production ($TKE \approx 1.22 \pm 0.52$ m^2 s^{-2} and $u* \approx 0.45 \pm 0.15$ m s^{-1} at $z \approx 2\ h_c$, cfr Table 1), amplifying vertical velocity fluctuations in the upper RSL (Figure 9d) [13,15].

At night, both TKE and u_* remain largely confined above canopy top, with very low values near the ground ($TKE \approx 0.04 \pm 0.04$ m^2 s^{-2} and $u* \approx 0.05 \pm 0.03$ m s^{-1} at $z \approx 0.07\ h_c$, cfr Table 1) indicating suppressed turbulent mixing and weak coupling between the surface and the overlying RSL under stable stratification, consistent with behavior observed in dense vegetated canopies [42,43]. The typical height of the TKE and $u*$ maxima (≈1–2 h_c, occasionally extending to ≈2.5–3 h_c under strong daytime forcing) reflects the balance between shear production and buoyancy within the canopy sublayer. Additional diagnostics of the shear and buoyancy terms of the TKE budget confirm that daytime turbulence is dominated by mechanical production with a secondary positive buoyancy contribution, whereas nighttime conditions exhibit weak shear and predominantly negative buoyancy. Across all surfaces, turbulence intensities decrease markedly within the UCL due to dissipation by roughness elements and obstruction of the mean flow [44]. Differences between surface types are generally modest, although above building-covered areas (Figure 9c–f) turbulent energy and momentum transport decay more steeply, reflecting strong structural sheltering.

Table 2. Mean ± standard deviation of thermodynamic variables—air temperature (*Ta*), sensible heat flux (*H*), latent heat flux (*LE*), and Bowen ratio (β)—for the full D03 domain and each surface class. Statistics are shown at three heights (pedestrian level, $z/hc = 1$, and $z/hc = 2$) and for daytime (10:00–18:00 LT) and nighttime (23:00–05:00 LT) periods. Values represent averages over all grid points of the corresponding surface type at the specified height.

Surface Type	***z/hc***	**Period**	T_a **(°C)**	***H*** **(W m^{-2})**	***Le*** **(W m^{-2})**	**β**
D03	0.07	Day	35.7 ± 1.8	52.4 ± 24.2	23.7 ± 10.5	2.2 ± 1.7
		Night	24.4 ± 2.6	−1.1 ± 1.1	1.2 ± 1.4	−1.1 ± 3.4
Asphalt	0.07	Day	35.8 ± 1.8	60.2 ± 27.7	12.6 ± 5.8	4.8 ± 2.9
		Night	24.5 ± 2.6	−0.4 ± 1.1	0.7 ± 1.8	−0.7 ± 4.8
Concrete	0.07	Day	35.6 ± 1.8	32.3 ± 20.3	14.1 ± 8.5	2.3 ± 3.3
		Night	24.4 ± 2.6	−1.6 ± 2.7	2.1 ± 4.7	−0.9 ± 3.2
Stones	0.07	Day	35.7 ± 1.8	44.5 ± 22.7	14.0 ± 6.9	3.2 ± 3.2
		Night	24.5 ± 2.6	−0.1 ± 2.5	1.8 ± 5.0	−0.2 ± 4.5
Buildings	0.07	Day	---	---	---	---
		Night	---	---	---	---
Trees	0.07	Day	35.5 ± 1.7	47.0 ± 20.2	60.3 ± 24.4	0.8 ± 0.4
		Night	24.0 ± 2.6	−3.3 ± 3.8	1.5 ± 4.1	−2.3 ± 2.1
Grass	0.07	Day	35.4 ± 1.6	40.9 ± 17.9	70.2 ± 30.0	0.6 ± 0.3
		Night	23.9 ± 2.6	−3.6 ± 2.4	1.7 ± 2.9	−2.0 ± 1.6
Bare	0.07	Day	35.4 ± 1.6	65.1 ± 29.2	122.3 ± 63.8	0.5 ± 0.7
		Night	23.2 ± 3.0	−3.8 ± 1.4	6.6 ± 3.0	−0.5 ± 0.1
D03	1	Day	35.3 ± 1.5	164.3 ± 49.6	30.2 ± 15.3	5.4 ± 3.0
		Night	24.9 ± 2.4	−3.8 ± 6.0	3.8 ± 11.5	−1.0 ± 3.6
Asphalt	1	Day	35.3 ± 1.5	167.3 ± 51.6	26.3 ± 14.5	6.3 ± 2.8
		Night	24.9 ± 2.4	−2.9 ± 5.3	3.3 ± 10.2	−0.9 ± 3.6
Concrete	1	Day	35.3 ± 1.5	149.8 ± 46.2	26.0 ± 13.9	5.8 ± 2.9
		Night	24.9 ± 2.4	−3.9 ± 6.1	3.5 ± 9.0	−1.1 ± 2.6
Stones	1	Day	35.3 ± 1.5	169.4 ± 51.4	28.1 ± 16.0	6.0 ± 3.0
		Night	24.9 ± 2.4	−3.9 ± 6.7	4.8 ± 11.8	−0.9 ± 3.8
Buildings	1	Day	35.3 ± 1.5	167.2 ± 46.9	20.5 ± 11.7	8.2 ± 2.3
		Night	24.9 ± 2.4	−5.6 ± 6.6	4.3 ± 13.5	−1.3 ± 4.3
Trees	1	Day	35.1 ± 1.5	160.3 ± 50.5	53.5 ± 22.2	3.0 ± 1.9
		Night	25.0 ± 2.4	−4.0 ± 8.0	5.1 ± 16.0	−0.8 ± 4.3
Grass	1	Day	35.1 ± 1.5	156.6 ± 48.5	61.3 ± 27.1	2.6 ± 2.1
		Night	24.9 ± 2.4	−3.5 ± 6.7	3.5 ± 11.0	−1.0 ± 5.2
Bare	1	Day	34.9 ± 1.4	146.1 ± 54.1	105.3 ± 47.4	1.4 ± 1.0
		Night	24.9 ± 2.4	−0.0 ± 8.7	2.5 ± 9.3	−0.1 ± 4.2
D03	2	Day	34.7 ± 1.4	213.1 ± 62.2	35.2 ± 22.6	6.1 ± 2.8
		Night	25.7 ± 2.0	−5.4 ± 7.5	6.3 ± 16.0	−0.8 ± 1.4
Asphalt	2	Day	34.7 ± 1.4	220.6 ± 64.9	33.8 ± 22.3	6.5 ± 2.7
		Night	25.7 ± 2.0	−5.5 ± 7.5	6.3 ± 16.3	−0.8 ± 2.9
Concrete	2	Day	34.7 ± 1.4	207.8 ± 61.1	35.1 ± 22.9	5.9 ± 3.0
		Night	25.8 ± 2.0	−5.4 ± 7.9	6.2 ± 15.4	−0.8 ± 1.6
Stones	2	Day	34.7 ± 1.4	209.7 ± 61.7	37.1 ± 25.6	5.7 ± 3.1
		Night	25.7 ± 2.0	−4.9 ± 7.2	5.2 ± 14.5	−0.9 ± 2.9
Buildings	2	Day	34.7 ± 1.4	209.4 ± 59.1	29.7 ± 20.9	7.1 ± 2.8
		Night	25.7 ± 2.0	−5.4 ± 7.2	6.1 ± 15.2	−0.8 ± 1.7
Trees	2	Day	34.7 ± 1.4	207.8 ± 64.8	48.1 ± 26.7	4.3 ± 2.9
		Night	25.7 ± 2.0	−6.1 ± 9.0	7.9 ± 20.9	−0.7 ± 2.8
Grass	2	Day	34.7 ± 1.4	206.0 ± 62.2	55.3 ± 28.8	3.7 ± 3.1
		Night	25.7 ± 2.0	−5.2 ± 7.7	6.3 ± 16.0	−0.8 ± 1.4
Bare	2	Day	34.6 ± 1.4	170.6 ± 57.7	80.5 ± 48.2	2.1 ± 3.0
		Night	25.8 ± 2.1	−1.0 ± 8.5	5.6 ± 20.5	−0.1 ± 4.4

In contrast to dynamical fields, thermodynamic variables exhibit stronger surface-dependent differences, as material thermal characteristics, heat storage and evapotranspiration directly modulate temperature and energy fluxes. The temporal and vertical evolutions of domain-averaged air temperature (T_a), sensible heat flux (H), and latent heat flux (LE) over D03 highlight (Figure 10) a clear diurnal cycle, with strong vertical variability across both the UCL and the RSL. Average air temperature in D03 shows intense daytime heating, with near-surface values reaching 36 °C in the afternoon, followed by gradual nocturnal cooling with minimum values near 24.5 °C, that reflect the persistent release of heat stored in the impervious materials dominating the district [45]. Sensible heat flux peaks just above rooftop level, around 2–3 h_c, coinciding with the region of maximum turbulent shear stress production, and decreases within the UCL. In contrast, latent heat flux exhibits stronger diurnal and vertical variability compared to H, with consistently low near-ground values reflecting the lack of evapotranspiration from the dominant impervious surfaces such as asphalt and concrete.

To better assess the role of surface characteristics, Figure 11 presents nocturnal and diurnal vertical profiles of normalized temperature, sensible heat, and latent heat fluxes for different surface types. Similarly to Figure 9, normalization was applied with respect to domain-averaged canopy-height statistics in D03. Distinct contrasts emerge between impervious and vegetated areas. Asphalt, concrete, and stone pavements exhibit systematically higher temperatures, while vegetation and bare soil remain comparatively cooler, underscoring their role in mitigating near-surface heating. At night, air temperatures above impervious surfaces remain more elevated (≈25 °C at $z/h_c = 0.07$) and relatively constant within the UCL, reflecting the retained heat and prolonged release of stored energy. On the other hand, vegetated areas exhibit cooler nocturnal values (≈24.0 °C at $z/h_c = 0.07$, Table 2), reflecting their reduced heat storage capacity.

Heat fluxes display a strong surface-related variability inside the UCL, with differences progressively weakening in the RSL above. Sensible heat flux is largest over hard surfaces during daytime, with H reaching 60 ± 28 W m^{-2} over asphalt, whereas vegetated patches exhibit milder values (trees: 47 ± 20 W m^{-2}; grass: 40 ± 18 W m^{-2}). During the night, H for urban materials approaches zero indicating a near neutral atmospheric stratifications [46], with values around -0.1 to -1.6 W m^{-2}, while H above rooftop surfaces shows more pronounced cooling (-5.6 ± 6.6 W m^{-2} at $z/h_c = 1$), consistent with the rapid radiative heat loss of roofing materials [16]. Latent heat fluxes provide the clearest signal of surface heterogeneity: tree-covered and grassy areas sustain markedly higher LE values, in particular during the day, due to evapotranspiration. At $z/h_c = 0.07$, daytime LE reaches 60 ± 24 W m^{-2} over trees and 70 ± 30 W m^{-2} over grass, whereas impervious surfaces contribute minimally (asphalt: 12.6 ± 5.8 W m^{-2}; concrete: 14.1 ± 8.5 W m^{-2}). This asymmetry persists at higher levels ($z/h_c = 1$ and 2), although with reduced magnitude, underscoring the influence of moisture fluxes in localized cooling above vegetated patches and in altering the vertical stability structure and energy partitioning within the UCL [47].

To further provide insight into the partitioning of available energy, Figure 12 reports nocturnal and diurnal vertical profiles of the Bowen ratio ($\beta = H/LE$) above the different surface types. The β profiles exhibit clear contrasts between impervious and vegetated surfaces, reflecting the strong control of surface thermal properties and moisture availability on energy partitioning. At night (Figure 12a), β is predominantly negative across most surfaces, since sensible heat fluxes are directed downward ($H < 0$) while latent heat fluxes remain weakly positive, sustained by residual evapotranspiration from vegetated areas. The negative β regime indicates radiatively cooled surfaces that absorb sensible heat from the air, with values near zero over impervious areas but larger over vegetated surfaces. Close to the ground ($z/h_c = 0.07$) nighttime mean β remains close to -1 over asphalt (-0.7)

and concrete (-0.9), but decreases more strongly above vegetation, reaching -2.3 over trees and -2.0 over grass (Table 2). Buildings exhibit the largest negative values of β (≈ -6), reflecting a stronger nocturnal cooling and limited surface moisture availability.

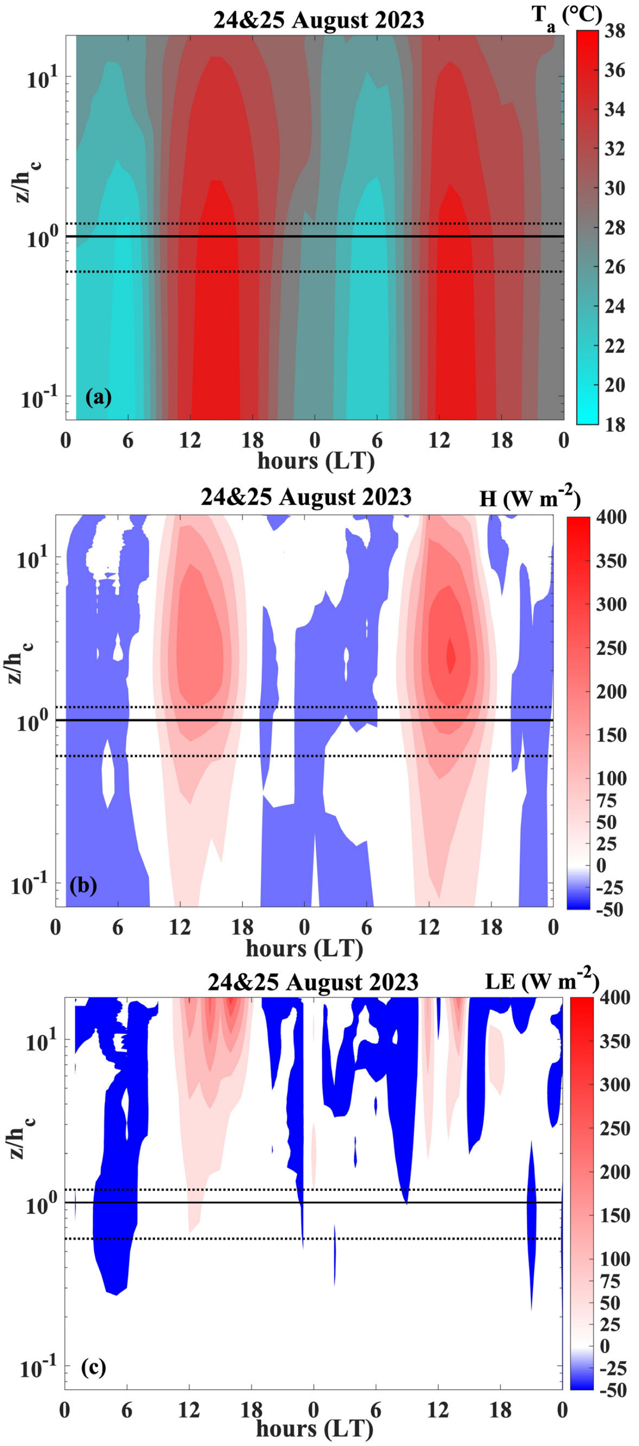

Figure 10. Temporal evolution of domain-averaged (**a**) air temperature T_a (°C), (**b**) sensible heat flux H (W m^{-2}), and (**c**) latent heat flux LE (W m^{-2}). in the Bolognina district from 24 to 25 August 2023. Values are averaged over the innermost domain (D03) and shown as a function of normalized height (z/h_c) and LT. Horizontal continuous and dotted lines mark, respectively, the median (14.5 m) and interquartile range (9–18 m) of the building height distribution. Time is LT (Local Standard Time, CET = UTC + 1 h).

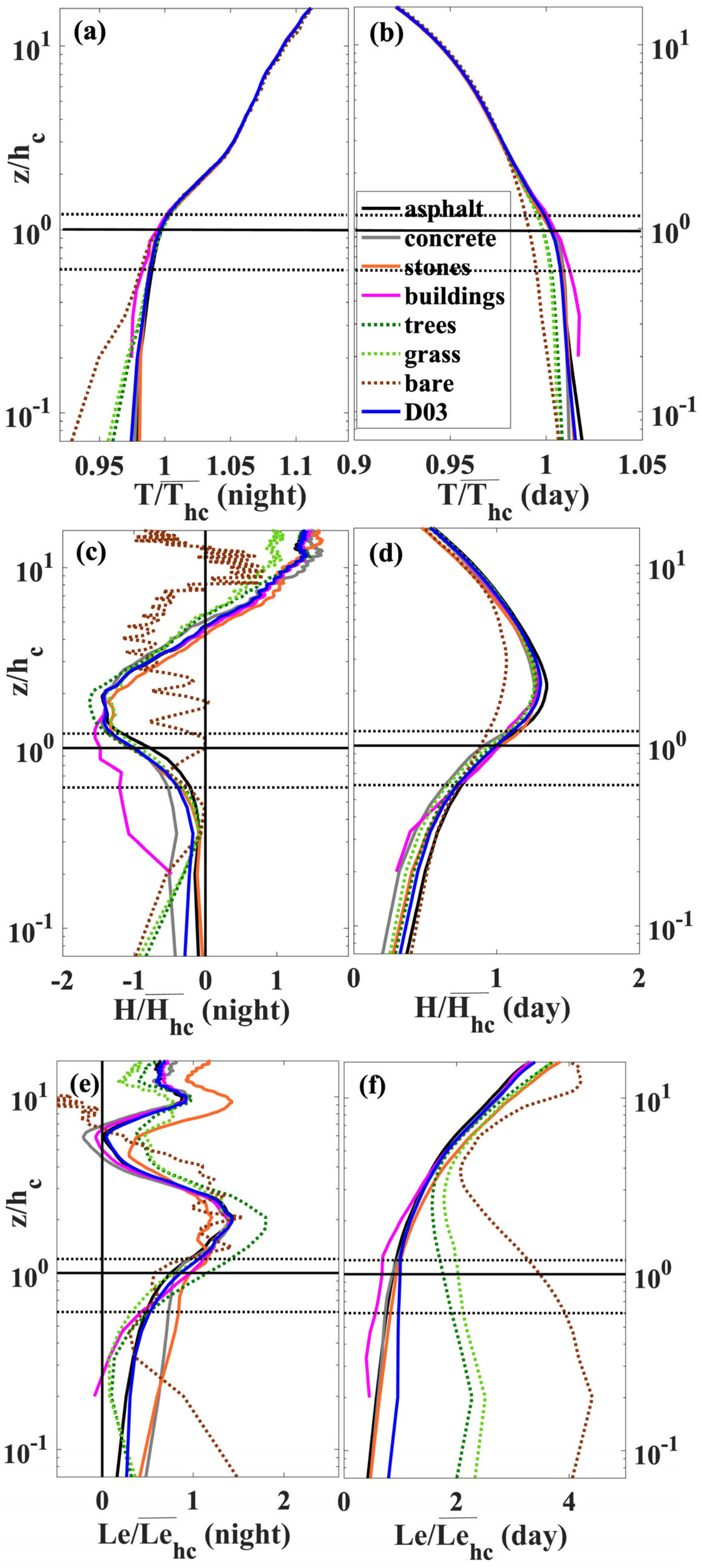

Figure 11. Nocturnal (**left panels**) and diurnal (**right panels**) average vertical profiles (**a**,**b**) normalized air temperature, (**c**,**d**) normalized sensible heat flux, and (**e**,**f**) normalized latent heat flux over different surface types in the Bolognina district. Normalization is performed with respect to the domain-averaged statistics at canopy height computed for the D03 innermost domain (indicated by the overbars). Solid black lines show the median building height (14.5 m), and dotted lines indicate the interquartile range (9–18 m) of the building height distribution.

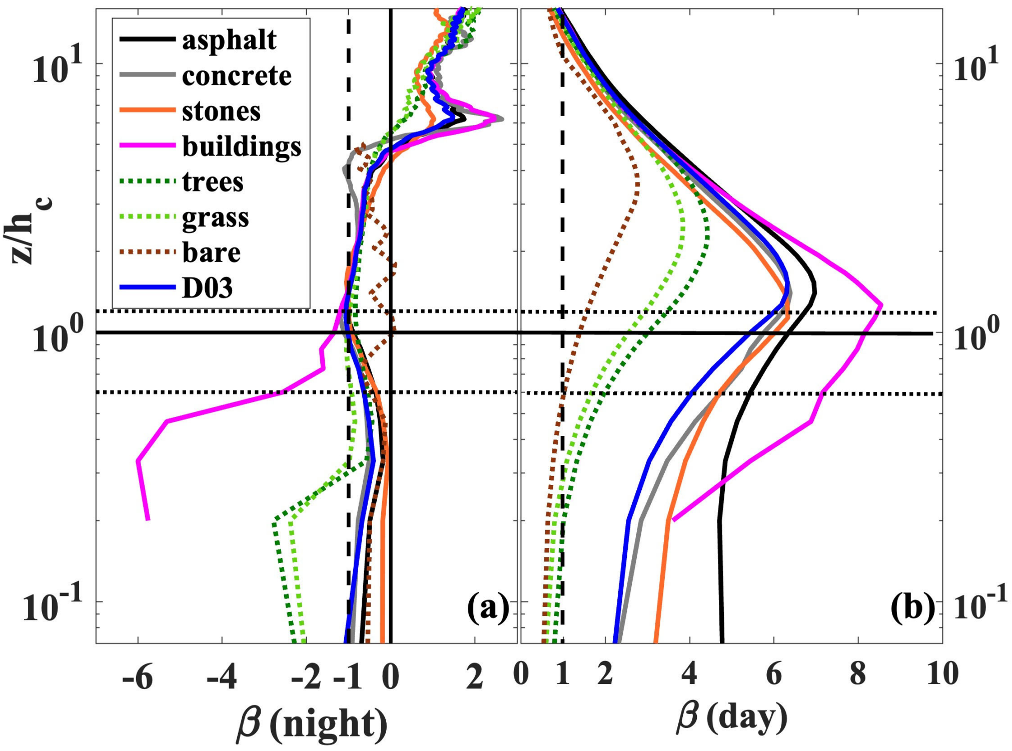

Figure 12. Nocturnal (**a**) and diurnal (**b**) average vertical profiles of Bowen ratio ($\beta = H/LE$) above different surface types in the Bolognina district. Vertical dashed lines show the ±1 values. Horizontal solid black lines show the median building height (14.5 m), and horizontal dotted lines indicate the interquartile range (9–18 m) of the building height distribution.

During daytime (Figure 12b), β becomes strongly positive, with values exceeding 5 above impervious surfaces such as asphalt and concrete (respectively, 6.5 and 5.9 at z/h_c = 2; Table 2), indicating a dominance of sensible over latent heat flux. This partitioning reflects the low soil and surface moisture typical of dense urban areas, where evapotranspiration is strongly suppressed [19,48]. Vegetated patches (grass and trees), in contrast, display significantly lower β values (<1 close to the surface) as evapotranspiration contributes more effectively to the energy balance and provides a moderate local cooling [10]. Mean daytime β is 0.8 over trees and 0.6 over grass at pedestrian height (z/h_c = 0.07), increasing less than above impervious surfaces with height as the influence of surface fluxes weakens. Above rooftops, the diurnal β remains elevated, reflecting strong heat release from roof materials and limited latent fluxes, although a decrease is observed above building height due to enhanced mixing with the overlying atmosphere. Consistently, roof-level β drops from 8.2 at z/h_c = 1 to 7.1 at z/h_c = 2, indicating progressive dilution of the surface thermal signals.

3.2. Daily Cycles of Surface Heat Exchange over Different Urban Surfaces

To complement the previous analysis of vertical and temporal patterns of dynamical and thermodynamic variables, the contribution of different surface types to the urban energy balance is examined. This section analyses the diurnal cycles of surface temperature and surface energy fluxes across various land-cover classes, emphasizing the role of material properties and moisture availability in modulating heat storage and release.

Figure 13 presents the diurnal evolution of the surface sensible heat flux (H_s), substrate heat flux (G), and surface temperature (T_s) for the main surface types in the Bolognina district. Values are extracted at the model surface level, following the actual topography of the urban elements rather than a fixed reference height, to capture the true variability of surface–atmosphere exchanges over impervious and vegetated surfaces. According to the PALM model system 6.0 technical documentation [24] and the urban surface model description [49], the ground heat flux (G) corresponds to the conductive heat flux at the interface between the surface and the first soil layer (diagnostic *g0*), computed using Fourier's law. Positive values indicate downward flux (heat storage), while negative values denote upward flux (release).

Roofs emerge as the dominant daytime sources of sensible heat (Figure 13a), with peaks around 250–280 Wm^{-2} around 14:00, according to other experimental measurements [16]. Unlike other impervious materials such as asphalt and concrete, roofs switch to net absorbers of heat at night (negative H_s values) which, together with the change in sign of G (Figure 13a,b), reflects the joint influence of efficient nocturnal longwave cooling and the release of heat stored in the substrate during daytime. The sharp reversal of G over roofs (Figure 13b) is particularly pronounced, moving from strong positive values during the day to negative values after sunset. This behavior is consistent with the PALM-4U single-layer slab representation, which lacks internal thermal stratification and therefore accelerates heat release once surface cooling begins.

Vegetated surfaces behave in a markedly different way: during the early morning they release some heat to the air, but by early afternoon their sensible heat flux becomes negative, indicating that they are absorbing energy from the atmosphere to sustain evapotranspiration (cf. Figure 11f). This effect strongly moderates near-surface warming over green areas.

The ground heat flux underpins these patterns by quantifying the net energy absorbed or released by the surface itself (Figure 13b). High daytime G over roofs, asphalt, and concrete coincides with large daytime sensible heat fluxes, whereas low values over vegetated areas reflect their capacity to divert energy toward latent heat. For roofs, the simplified slab model amplifies diurnal swings: during the day, the homogeneous layer stores heat efficiently, producing large positive G; at night, the absence of multilayer buffering leads to rapid cooling and strong negative G, as the stored energy is quickly released to the surface and then to the atmosphere. The pronounced negative G at night over impervious surfaces (≈ -50 Wm^{-2}) underscores their role as heat reservoirs, releasing stored energy and contributing to the persistence of nocturnal urban warmth.

Urban surface temperature responds directly to these fluxes (Figure 13c). Roofs reach extreme daytime values (≈71–72 °C) due to high absorption and negligible evapotranspiration, while asphalt, stones and concrete follow a similar but less intense pattern (maxima equal to 50 °C, 44 °C and 42 °C, respectively). In contrast, trees and grass maintain significantly cooler surfaces throughout the day (maxima ≈ 37 °C). After sunset, the rapid decline of $\mathrm{T_s}$ over roofs (down to ≈16–19 °C) mirrors the strong negative G and the simplified thermal representation. Other impervious materials (asphalt and concrete) cool more slowly and stabilize at markedly higher nocturnal temperatures (approximately 5–6 °C above vegetation), reflecting their greater heat-storage capacity and slower release. The nocturnal convergence of T_s between roofs and vegetated areas coincides with a marked reduction and a reversal of sensible and substrate heat fluxes over roofs, indicating a fast release of stored energy after sunset. In contrast, the persistently higher nocturnal T_s over asphalt and concrete is consistent with their larger negative G values at night and reduced heat dissipation, which sustain elevated surface and near-surface air temperatures.

The spatial distribution of surface temperature further illustrates the strong local heterogeneity of the urban thermal environment (Figure 14). At 11:00 LT, impervious surfaces such as rooftops, asphalt, and concrete exhibit markedly higher temperatures than vegetated patches, reaching 60–70 °C in some areas (according to Figure 13c), whereas tree-covered and shaded zones remain substantially cooler (35–25 °C). At 23:00, surface temperatures decrease across the domain but retain significant spatial variability due to differences in the thermal inertia and heat release of urban materials. The maps also reveal the influence of urban geometry in modulating T_s through shading and radiative trapping, producing distinct microclimatic patterns that vary with the time of day. These results confirm the role of building arrangement and sky openness in shaping intra-urban thermal contrasts.

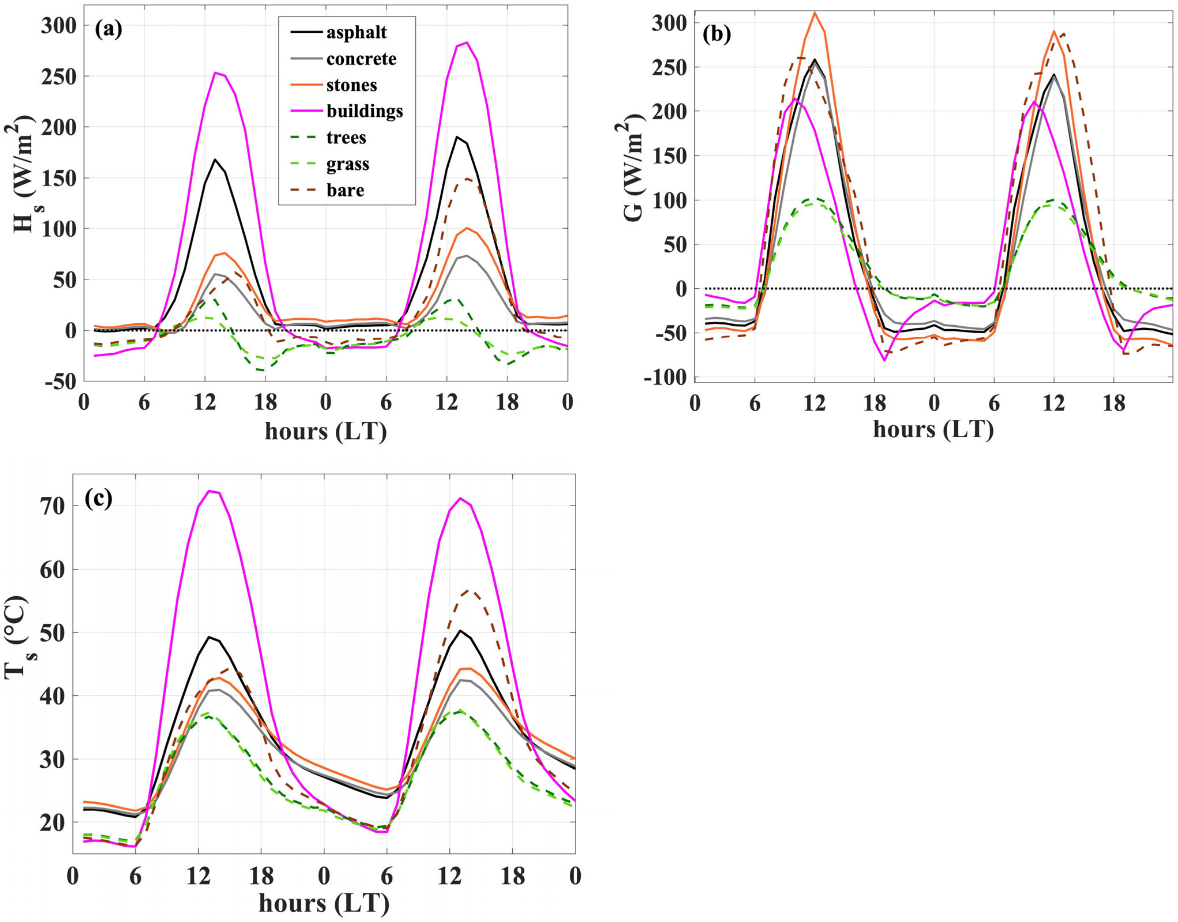

Figure 13. Diurnal evolution of (**a**) surface sensible heat flux (H_s, W m^{-2}), (**b**) substrate heat flux (G, W m^{-2}), and (**c**) surface temperature (T_s, °C) for the main surface types in the Bolognina district. Continuous and dotted lines refer to impervious and vegetated surfaces, respectively. Values are extracted at the model surface level, following the actual topography of the urban elements. Results are shown separately for asphalt, concrete, paving stones, rooftops, bare soil, grass, and tree-covered areas. Time is LT (Local Standard Time, CET = UTC + 1 h).

Figure 15 shows the normalized probability density functions (pdfs) of surface temperature for the two snapshots displayed in Figure 14. Rooftop grid cells were excluded to focus on street-level conditions. At 11:00 LT, the distribution is further stratified into 'sunlit' and 'shaded' surfaces (Figure 15a). Shade classification was performed using the instantaneous radiative field simulated by PALM-4U: grid cells receiving more than 30 W m^{-2} of direct shortwave radiation were defined as 'sunlit', while all others were considered 'shaded'. This criterion captures radiative obstruction from buildings and vegetation. Sensitivity tests using thresholds between 20 and 50 W m^{-2} produced qualitatively identical shapes of the T_s probability distribution, confirming the robustness of the classification. The resulting pdfs reveal distinct thermal regimes with distinct peaks between approximately 30–32 °C, 40–42 °C, and above 50 °C. The 'shaded' population forms the dominant cool peak around 30–32 °C, associated with deep canyon shadows and dense vegetation. Interestingly, the sunlit class also contains a cool mode in this range, primarily corresponding to sun-exposed vegetation. Warmer peaks (40–42 °C) reflect sunlit concrete and paving stones, while the hottest temperatures (>50 °C) originate almost exclusively from sunlit asphalt. The contrast between the coolest shaded surfaces and the warmest sunlit asphalt approaches 25–30 °C at this hour highlighting the strong surface thermal contrasts that pedestrians may encounter within short distances during the day. Although diffuse illumination can produce occasional borderline cases, their fraction is very small and does not affect the multimodal structure of the distributions.

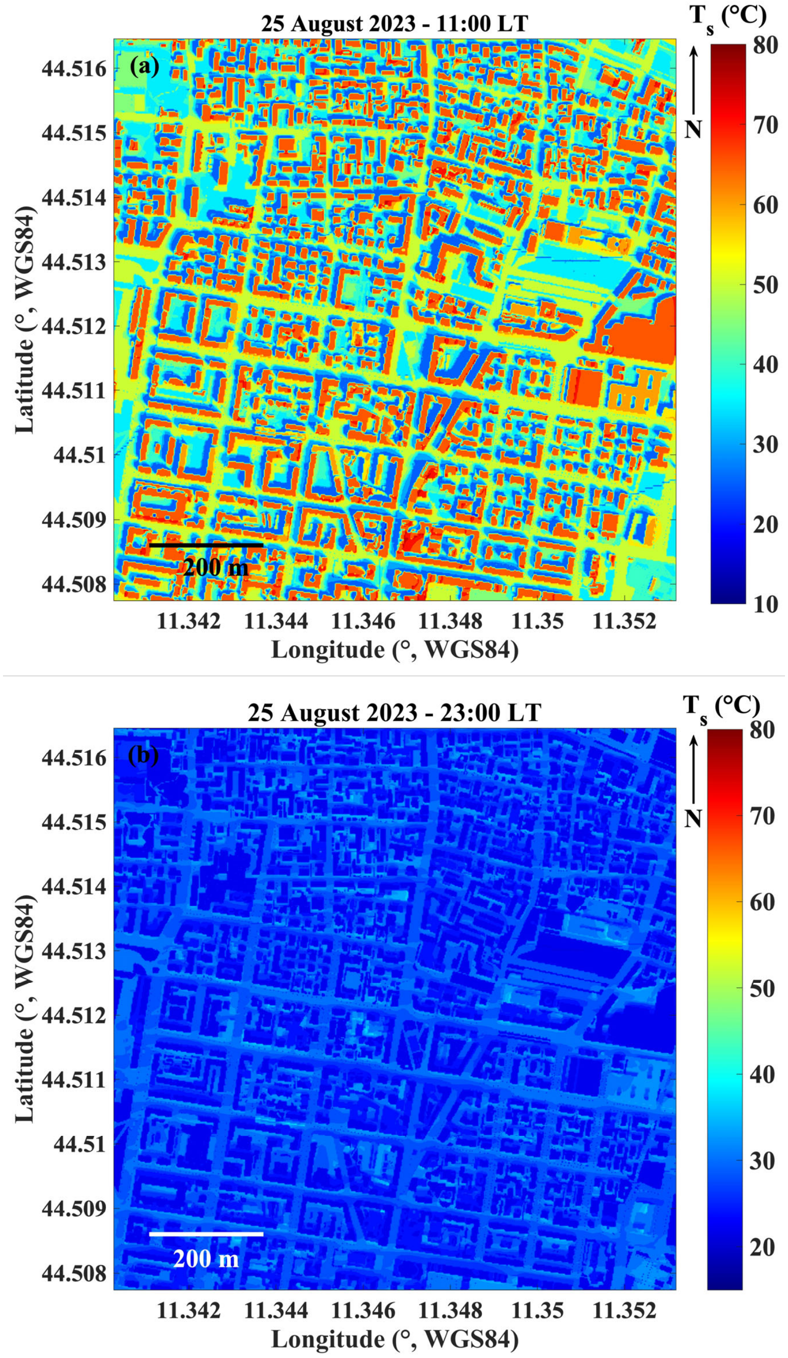

Figure 14. Spatial distribution of simulated urban surface temperature (T_s, °C) over the Bolognina district on 25 August 2023 at 11:00 LT (**a**) and 23:00 LT (**b**). Time is LT (Local Standard Time, CET = UTC + 1 h).

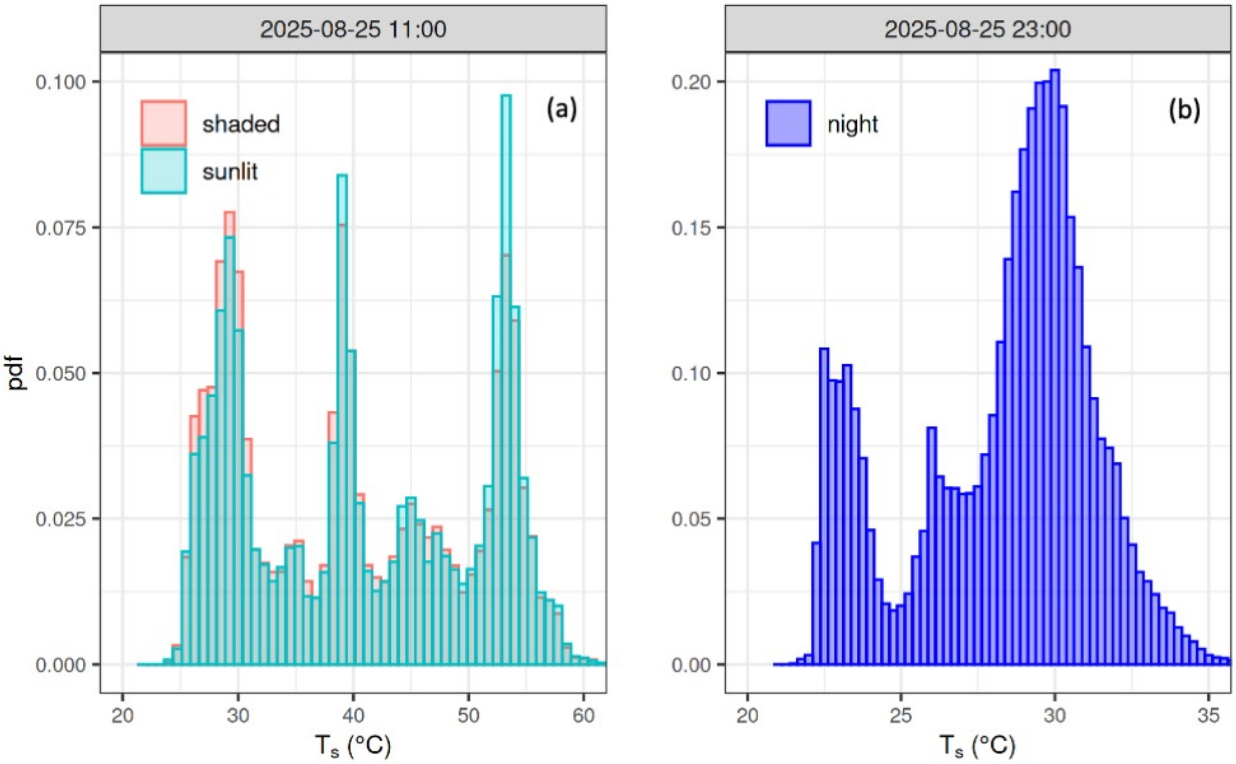

Figure 15. Normalized probability density functions (pdfs) of surface temperature T_s for (**a**) 11:00 LT and (**b**) 23:00 LT on 25 August 2023. Rooftop cells are excluded. At 11:00 LT, the distribution is separated into 'sunlit' and 'shaded' surfaces using the modeled direct shortwave irradiance (>30 W m^{-2} corresponding to 'sunlit'). Time is LT (Local Standard Time, CET = UTC + 1 h).

By contrast, at 23:00 (Figure 15b), the pdf narrows and shifts toward lower temperatures reflecting the general cooling of the urban surfaces after sunset. Nevertheless, two modes remain visible: one at the lower end (~23 °C) corresponding to vegetated or shaded areas that cool more efficiently, and another around ~30 °C linked to impervious surfaces (especially asphalt and concrete) that retain heat longer overnight. The nocturnal thermal spread is still about 6–8 °C between the coolest and warmest surfaces, underscoring the persistence of heat stored in impervious materials and explaining the elevated near-surface air temperatures and the reduced nighttime thermal comfort typical of dense urban districts. This day–night comparison highlights the amplitude of intra-urban thermal contrasts at pedestrian level. Although temperatures decrease after sunset, relative differences between cool vegetated surfaces and warm impervious materials remain appreciable throughout the night [19]. While direct observations of T_s were not available for validation, the model sensitivity to radiative and hydrological parameters has been evaluated. A perturbation of ±0.05 in albedo alters absorbed shortwave radiation by ±40 W m^{-2}, corresponding to an expected T_s change of 1–2 °C under daytime high-Bowen-ratio conditions—values consistent with observational studies of albedo modification [50,51]. Soil-moisture variations similarly produce temperature shifts of a few degrees, but do not diminish the large contrast (>20 °C) between vegetated and impervious surfaces [52,53]. Hence, while absolute magnitudes may shift slightly, the spatial patterns and their physical interpretation remain robust.

After assessing surface-temperature contrasts among materials and shading conditions, we next evaluate their implications for pedestrian thermal exposure. Figure 16 presents the bio-PET (Physiologically Equivalent Temperature) probability density functions separately for sunlit and shaded locations at pedestrian level (z/h_c = 0.07). The sunlit and shaded classes are defined consistently with the classification applied to T_s (Figure 15). The daytime distribution of bio-PET (Figure 16a) exhibits a multimodal structure, with peaks spanning approximately 30–35 °C and 40–55 °C, reflecting the combined effects of radiative exposure, surface temperature contrasts, and very low wind speeds within the canyon. The coolest peak is mainly associated with shaded or densely vegetated areas, while the and hottest modes are associated with sun-exposed asphalt, respectively. This emphasizes that pedestrians may experience differences exceeding 20 °C in PET within only a few meters, consistent with the strong thermal gradients identified in the surface-temperature PDFs. At night (Figure 16b), the bio-PET distribution narrows substantially and shifts toward lower values (mostly 24–28 °C). Although absolute PET differences become smaller at night, the relative contrasts between vegetated and impervious surfaces persist, mirroring the spatial patterns previously described for both T_s and near-surface air temperature. These results underline that nocturnal heat retention continues to modulate pedestrian-level thermal exposure and contributes to reduced nighttime comfort in dense urban districts.

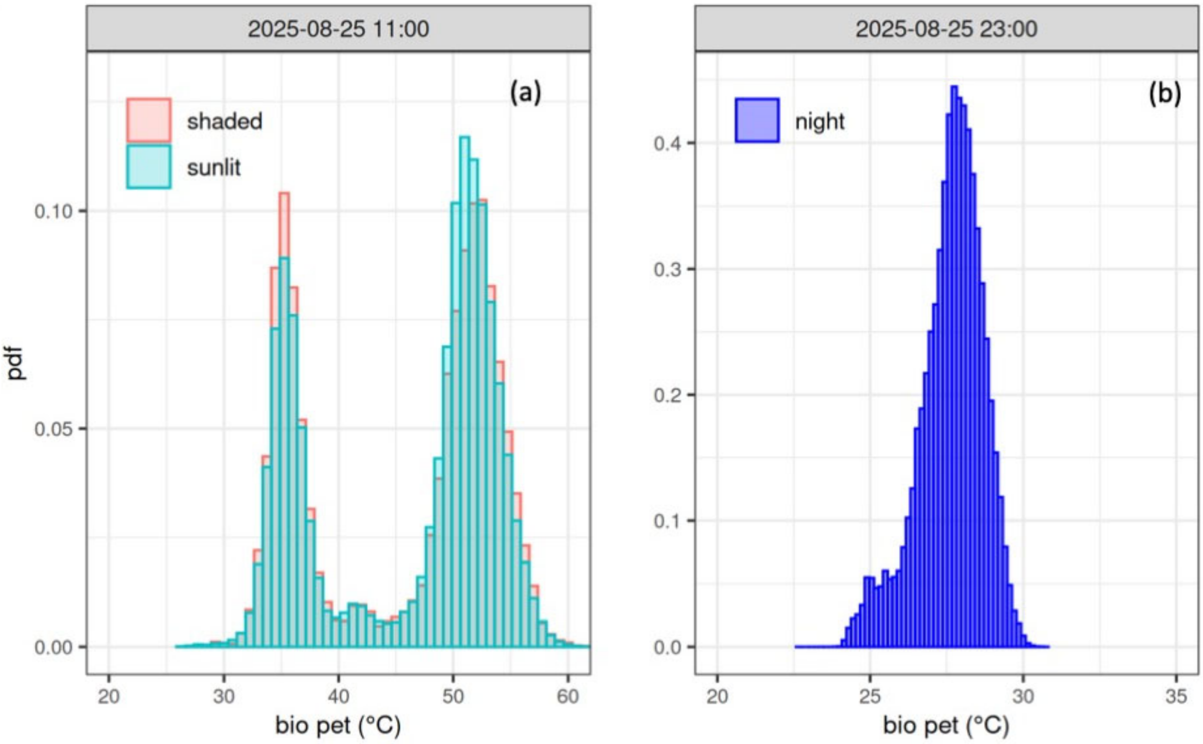

Figure 16. Normalized probability density functions (pdfs) of bio-PET (Physiologically Equivalent Temperature) for (**a**) 11:00 LT and (**b**) 23:00 LT on 25 August 2023. Rooftop cells are excluded. At 11:00 LT, the distribution is separated into 'sunlit' and 'shaded' surfaces using the modeled direct shortwave irradiance (>30 W m^{-2} corresponding to 'sunlit'). Time is LT (Local Standard Time, CET = UTC + 1 h).

3.3. Microclimatic Impact in the Urban and Roughness Sublayers

Local differences in material properties, moisture availability, and surface geometry generate distinct thermal regimes that extend upward from the surface into the UCL and RSL. This section explores the microclimatic imprint of different surface types on air temperature by analyzing their deviations from the domain-averaged conditions, thereby revealing how individual land covers contribute to intra-urban thermal variability in the UCL and above the urban canopy top.

Figure 17 shows the temporal and vertical evolution of air-temperature anomalies (ΔT_{air}), defined as the difference between the mean temperature of a specific surface class and the domain-averaged temperature at the same height in D03. Thus, for each time t and vertical level z, ΔT_{air} quantifies how much air over a given surface type (e.g., asphalt, grass, trees) is warmer (reds) or cooler (blues) relative to the domain-wide background state.

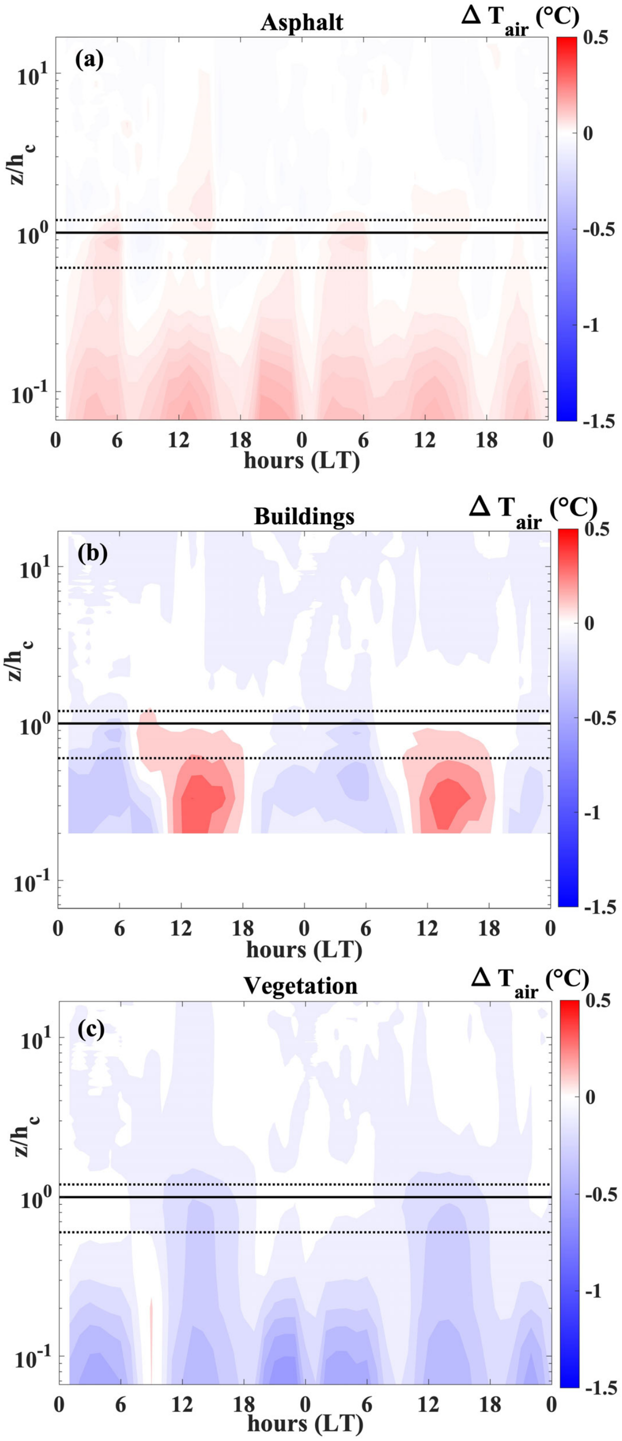

Figure 17. Temporal and vertical evolution of air-temperature anomalies (ΔT_{air}, °C) over (**a**) asphalt, (**b**) building roofs, and (**c**) vegetation. Anomalies are defined as the difference between the surface-class mean air temperature and the domain-averaged air temperature at the same height. The color scale ranges from -1.5 to $+0.5$ °C, with warm colors indicating air warmer than the domain mean and cool colors indicating cooler air. Horizontal solid and dotted lines denote, respectively, the median building height (14.5 m) and the interquartile range (9–18 m) of the building-height distribution. Time is LT (Local Standard Time, CET = UTC + 1 h).

Over impervious surfaces, particularly asphalt (Figure 17a), positive temperature anomalies dominate the UCL during both daytime and nighttime, extending from the surface up to and above the median building height. This persistent warming reflects asphalt's low albedo, high thermal mass, and negligible evapotranspiration, which together promote strong sensible heat fluxes into the atmosphere. Concrete and stone surfaces exhibit a similar but less pronounced pattern, consistent with their intermediate thermal properties. Building roofs (Figure 17b) also show significant positive anomalies during daytime and negative anomalies at night, typically confined to the canopy-top region, indicating intense but more localized heating/cooling linked to the low thermal inertia of roofing materials like clay or concrete tiles.

In contrast, vegetated areas (Figure 17c) display widespread negative temperature anomalies during the day, with cooler air extending vertically into the UCL. This pattern highlights the cooling role of evapotranspiration and shading, which both limit near-surface heating and reduce sensible heat transfer to the atmosphere. The cooling signature persists attenuated into the night, demonstrating vegetation's capacity to delay and moderate urban warming.

These qualitative patterns are supported by the quantitative summary reported in Table 3. The first block of rows (highlighted by orange color and asterisks) displays the mean anomalies of the surface temperatures (T_s, shown in Figure 13c), whereas the further blocks refer to the air temperature anomalies above the different materials (ΔT_{air}, first evaluated 1 m above the surface, marked with a plus). Surface-temperature anomalies exhibit the strongest contrasts: sunlit roofs show the highest daytime surface heating, with ΔT_s reaching +29.8 ± 5.55 °C, while vegetated surfaces remain up to 9 °C cooler than the domain mean at the same time. Asphalt displays intermediate heating ($\Delta T_s \approx +1.1 \pm 0.98$ °C during daytime and +2.53 ± 0.17 °C at night), reflecting its high thermal inertia.

Air-temperature anomalies are substantially smaller in magnitude. Close to the surfaces ($z/h_c \approx 0.07$–0.2) daytime ΔT_{air} remains within +0.14 °C over asphalt, +0.21 °C over roofs, and about -0.31 °C above vegetation. Nighttime differences are similarly modest ($|\Delta T_{air}| < 0.5$ °C). At greater heights ($z/h_c \geq 1$), air-temperature anomalies converge toward zero ($|\Delta T_{air}| < 0.1$ °C), confirming the rapid vertical decay of surface-driven thermal contrasts and their effective homogenization by turbulent mixing above the urban canopy layer. The rapid attenuation of temperature anomalies with height is consistent with efficient turbulent mixing in the upper part of the canopy layer and the overlying roughness sublayer. Using representative daytime values of vertical velocity fluctuations ($\sigma_w \approx 0.6$ m s^{-1}) and a characteristic mixing length of order h_c, the corresponding mixing timescale $\tau_{mix} \approx L/\sigma_w$ is on the order of 20–30 s. Such short timescales support the interpretation that thermal anomalies originating at the surface are quickly homogenized above 2–3 h_c, in agreement with the near-zero ΔT_{air} values observed in our vertical profiles.

These results show how material properties, moisture availability, and surface geometry combine to produce distinct microclimatic regimes within the urban environment. Impervious surfaces act as daytime heat sources and nighttime heat reservoirs, whereas vegetated areas provide sustained cooling through evapotranspiration.

Table 3. Median daytime and nighttime temperature anomalies (ΔT, °C) for each surface class at selected normalized heights. Values marked with * refer to surface temperature (T_s) (first block highlighted with orange color), evaluated at z = 0 for impervious and vegetated surfaces and at $z \approx 0.07\ h_c$ for roofs. All other entries represent air-temperature anomalies (ΔT_{air}). Values marked with + correspond to the first air layer one meter above the surface ($z \approx 0.07\ h_c$ for impervious and vegetated surfaces and $z \approx 0.2\ h_c$ for roofs). Reported values include median ± standard deviation.

Surface Type	z/hc	Period	ΔT (°C)
Asphalt	0 *	Day	1.14 ± 0.98
		Night	2.53 ± 0.17
Buildings	0.07 *	Day	29.8 ± 5.55
		Night	−4.84 ± 0.75
Vegetation	0 *	Day	−9.03 ± 2.21
		Night	−2.45 ± 0.59
Asphalt	0.07 +	Day	0.14 ± 0.04
		Night	0.12 ± 0.04
Buildings	0.2 +	Day	0.21 ± 0.12
		Night	−0.08 ± 0.06
Vegetation	0.07 +	Day	−0.31 ± 0.11
		Night	−0.44 ± 0.11
Asphalt	1	Day	0.02 ± 0.02
		Night	0.02 ± 0.03
Buildings	1	Day	0.06 ± 0.02
		Night	−0.04 ± 0.05
Vegetation	1	Day	−0.16 ± 0.03
		Night	0.04 ± 0.02
Asphalt	2	Day	0.02 ± 0.02
		Night	−0.01 ± 0.01
Buildings	2	Day	0.01 ± 0.01
		Night	−0.00 ± 0.01
Vegetation	2	Day	−0.04 ± 0.02
		Night	0.00 ± 0.02
Asphalt	3	Day	0.0 ± 0.02
		Night	0.0 ± 0.01
Buildings	3	Day	0.00 ± 0.00
		Night	0.00 ± 0.01
Vegetation	3	Day	−0.00 ± 0.02
		Night	−0.00 ± 0.02

4. Discussion and Conclusions

This study employed meter-scale Large-Eddy Simulations using the coupled MOLOCH–PALM-4U model system to investigate the spatial and temporal variability of turbulence, energy partitioning, and air temperature across different urban surface types in a district of Bologna during a summer heatwave of 2023. The results demonstrate that high-resolution LES can resolve the fine-scale dynamical and thermodynamical structure of the Urban Canopy Layer and Roughness Sublayer, providing physically consistent insights into processes not captured by mesoscale models and sparse observations.

Across the diurnal cycle, turbulence exhibits a robust vertical organization: wind speed, turbulent kinetic energy, and friction velocity peak between roughly two and three times the median building height, where strong vertical shear promotes turbulence production. Within the UCL, turbulence intensities remain comparatively weak due to the dense and heterogeneous morphology. Thermodynamic quantities show even stronger surface dependence. Impervious materials (asphalt, concrete, stone, and rooftops) exhibit high daytime sensible heat fluxes, weak latent heat fluxes, and substantial heat storage, generating warm near-surface air and positive temperature anomalies extending up to canopy top. Vegetated areas, in contrast, sustain higher latent heat fluxes and systematically cooler conditions, producing negative air-temperature anomalies that persist into the night. These microclimatic signatures progressively weaken with height and largely vanish in the upper UCL and RSL as turbulent mixing homogenizes the air mass.

The distributions of surface and near-surface temperature underline the strong thermal heterogeneity at pedestrian level. Daytime multimodal patterns separate cool vegetated and shaded surfaces from much hotter sun-exposed impervious materials, while nocturnal distributions reflect the slower heat release of high-inertia materials. The implications of these thermal disparities for human exposure are further quantified through the bio-PET metric, which confirms that vegetated and shaded environments can reduce perceived thermal stress by more than one comfort class relative to sunlit asphalt or stone, especially during daytime peak heating. This alignment between physical temperature fields and bio-PET reinforces the functional relevance of localized cooling induced by vegetation and shading.

Together, these findings show that the interplay between material thermal properties, moisture availability, and urban geometry produces strong spatial and temporal contrasts in surface energy exchanges—and controls intra-urban thermal variability at the scale most relevant to human exposure. This fine-scale variability is crucial for understanding intra-urban heat dynamics and for informing climate-resilient urban planning strategies aimed at mitigating heat stress and enhancing thermal comfort. Vegetated surfaces—particularly trees—consistently generate strong cooling signals, indicating that shading and evapotranspiration remain key levers for reducing pedestrian-level heat. Impervious surfaces with high daytime Bowen ratios and strong nocturnal ground-heat release represent priority targets for mitigation through reflective coatings, permeable materials, or shading interventions. Rooftops, which reach the highest daytime temperatures, offer substantial potential for cool-roof or green-roof technologies. The present analysis examined mean profiles of vertical wind speed standard deviation and sensible heat flux. These findings indicate that roof-generated heat is primarily ventilated upward into the roughness sublayer, rather than recirculated within street canyons. However, such diagnostics cannot capture intermittent downward intrusions. To address this gap, a forthcoming study will investigate turbulent dynamics in greater detail, leveraging virtual high-frequency outputs from PALM. This will enable quadrant decomposition and wavelet-based techniques to quantify coherent structures and assess their role in pedestrian-level thermal exposure.

Beyond this methodological limitation, the analysis is constrained by its focus on a single heatwave episode (24–25 August 2023). Although the coupled system was evaluated against in situ observations and Landsat-8 LST, direct flux measurements were not available. Moreover, the offline MOLOCH–PALM-4U coupling inherits assumptions from mesoscale forcing and omits feedbacks to the larger-scale flow, which may influence the representativeness of the simulated dynamics.

Another important limitation concerns the exclusion of anthropogenic heat and irrigation in the PALM-4U configuration. This modeling choice allowed us to isolate biophysical surface responses driven by material properties and radiative–hydrological coupling, but it inevitably reduces the realism of the simulated energy balance during a heatwave in a dense, mixed-use district. Published estimates indicate that anthropogenic heat emissions typically contribute 20–70 W m^{-2} in European cities, with peaks exceeding 100 W m^{-2} during maximum air-conditioning demand in summer periods [54,55]. These fluxes can increase near-surface air temperature by approximately 0.5–1.5 °C and substantially enhance sensible heat, particularly within street canyons [56]. Recent studies further emphasize that anthropogenic heat can intensify urban warming and even increase the frequency of extreme heat events in Europe, highlighting sustained fluxes above 50–100 W m^{-2} in dense districts [57,58]. Conversely, urban irrigation and watering of vegetated areas may increase latent heat fluxes by 20–40 W m^{-2} and reduce local air temperature by as much as 1 °C through enhanced evapotranspiration [59,60]. Therefore, the omission of anthropogenic heat likely leads to a conservative underestimation of warming over impervious surfaces, while the omission of irrigation may lead to an underestimation of cooling over vegetated patches. As a result, the simulated thermal contrast between impervious and vegetated surfaces is likely attenuated relative to fully realistic urban conditions. Nonetheless, these relative spatial contrasts remain informative for mechanistic interpretation, while absolute temperatures may be biased. Quantifying these competing effects will be a central focus of future work, in which PALM-4U will be extended to include anthropogenic heat injection and irrigation schemes and tested across multiple heat events.

Author Contributions: Conceptualization, D.C., L.M., U.G. and D.d.V.B.; Methodology, D.C., L.M. and U.G.; Software, L.M., T.C.L., O.D. and D.d.V.B.; Formal analysis, D.C.; Investigation, D.C., L.M. and D.d.V.B.; Resources, T.C.L.; Data curation, D.C., L.M., T.C.L., G.V., E.F. and D.d.V.B.; Writing—original draft, D.C.; Writing—review & editing, D.C., L.M., U.G., D.d.V.B. and E.F.; Supervision, L.M. and U.G.; Funding acquisition, T.C.L. All authors have read and agreed to the published version of the manuscript.

Funding: This research was funded by European Union— National Recovery and Resilience Plan (NRRP), Mission 4 Component 2 Investment 1.4—Call for tender No. 3138 of 16 December 2021, rectified by Decree n.3175 of 18 December 2021 of Italian Ministry of University and Research funded by the European Union—NextGenerationEU; Project code CN00000033, Concession Decree No. 1034 of 17 June 2022 adopted by the Italian Ministry of University and Research, CUP B83C22002930006 Project title "National Biodiversity Future Center—NBFC". The APC was waived.

Data Availability Statement: The raw data supporting the conclusions of this article will be made available by the authors on request.

Acknowledgments: The authors gratefully acknowledge the CINECA High Performance Computing (HPC) facility for providing the computational resources and support for this project. This work has been funded by UNITECH INDACO, which is an HPC project at the state University of Milan (Italy). and the ISCRA-C program, project IsCc4 (grant ID: AUSM-LES), within the science domain of Earth and Climate Science. The authors thank Fabrizio Roccato for his invaluable technical support in preparing the input data for the PALM-4U model.

Conflicts of Interest: The authors declare no conflict of interest.

References

1. UN DESA. *World Urbanization Prospects: The 2018 Revision*; United Nations: New York, NY, USA, 2018.
2. Oke, T.R.; Mills, G.; Christen, A.; Voogt, J.A. *Urban Climates*; Cambridge University Press: Cambridge, UK, 2017. [CrossRef]
3. Arnfield, A.J. Two Decades of Urban Climate Research: A Review of Turbulence, Exchanges of Energy and Water, and the Urban Heat Island. *Int. J. Climatol.* **2003**, *23*, 1–26. [CrossRef]
4. Best, M.J.; Grimmond, C.S.B. Key Conclusions of The First International Urban Land Surface Model Comparison Project. *Bull. Am. Meteorol. Soc.* **2015**, *96*, 805–819. [CrossRef]

5. Ferreira, M.J.; Duarte, D.H.S. Exploring the relationship between urban form, land surface temperature and vegetation cover in a subtropical megacity. *Urban Clim.* **2019**, *27*, 105–123. [CrossRef]
6. Li, D.; Bou-Zeid, E.; Oppenheimer, M. The effectiveness of cool and green roofs as urban heat island mitigation strategies. *Environ. Res. Lett.* **2019**, *14*, 094007. [CrossRef]
7. Winbourne, J.B.; Jones, T.S.; Garvey, S.M.; Harrison, J.L.; Wang, L.; Li, D.; Templer, P.H.; Hutyra, L.R. Tree Transpiration and Urban Temperatures: Current Understanding, Implications, and Future Research Directions. *BioScience* **2020**, *70*, 576–588. [CrossRef]
8. Li, D.; Wang, L.; Liao, W.; Sun, T.; Katul, G.; Bou-Zeid, E.; Maronga, B. Persistent Urban Heat. *Sci. Adv.* **2024**, *10*, eadj7398. [CrossRef]
9. Yang, J.; Wu, Z.; Menenti, M.; Wong, M.S.; Xie, Y.; Zhu, R.; Abbas, S.; Xu, Y. Impacts of urban morphology on sensible heat flux and net radiation exchange. *Urban Clim.* **2023**, *50*, 101588. [CrossRef]
10. Back, Y.; Bach, P.M.; Santamouris, M.; Rauch, W.; Kleidorfer, M. Role of surface energy fluxes in urban overheating under buoyancy-driven atmospheric conditions. *J. Geophys. Res. Atmos.* **2024**, *129*, e2023JD039723. [CrossRef]
11. Svensson, M.K. Sky View Factor Analysis—Implications for Urban Air Temperature Differences. *Meteorol. Appl.* **2004**, *11*, 201–211. [CrossRef]
12. Roth, M. Review of atmospheric turbulence over cities. *Q. J. R. Meteorol. Soc.* **2000**, *126*, 941–990. [CrossRef]
13. Rotach, M.W.; Vogt, R.; Bernhofer, C.; Batchvarova, E.; Christen, A.; Clappier, A.; Feddersen, B.; Gryning, S.-E.; Martucci, G.; Mayer, H.; et al. BUBBLE—An Urban Boundary Layer Meteorology Project. *Theor. Appl. Climatol.* **2005**, *81*, 231–261. [CrossRef]
14. Christen, A.; Rotach, M.W.; Vogt, R. The Budget of Turbulent Kinetic Energy in the Urban Roughness Sublayer. *Bound.-Layer Meteorol.* **2009**, *131*, 193–222. [CrossRef]
15. Zou, J.; Zhou, B.; Sun, J. Impact of Eddy Characteristics on Turbulent Heat and Momentum Fluxes in the Urban Roughness Sublayer. *Bound.-Layer Meteorol.* **2017**, *164*, 39–62. [CrossRef]
16. Salmond, J.A.; Roth, M.; Oke, T.R.; Christen, A.; Voogt, J.A. Can Surface-Cover Tiles Be Summed to Give Neighborhood Fluxes in Cities? *J. Appl. Meteorol. Climatol.* **2012**, *51*, 133–149. [CrossRef]
17. Ziter, C.D.; Pedersen, E.J.; Kucharic, C.J.; Turner, M.G. Scale-dependent interactions between tree canopy cover and impervious surfaces reduce daytime urban heat during summer. *Proc. Natl. Acad. Sci. USA* **2019**, *116*, 7575–7580. [CrossRef] [PubMed]
18. Nazarian, N.; Fan, J.; Sin, T.; Norford, L.; Kleissl, J. Predicting outdoor thermal comfort in urban environments: A 3D numerical model for standard effective temperature. *Urban Clim.* **2017**, *20*, 251–267. [CrossRef]
19. Nadeau, D.F.; Brutsaert, W.; Parlange, M.B.; Bou-Zeid, E.; Barrenetxea, G.; Couach, O.; Boldi, M.O.; Selker, J.S.; Vetterli, M. Estimation of urban sensible heat flux using a dense wireless network of observations. *Environ. Fluid Mech.* **2009**, *9*, 635–653. [CrossRef]
20. Letzel, M.O.; Krane, M.; Raasch, S. High resolution urban large-eddy simulation studies from street canyon to neighbourhood scale. *Atmos. Environ.* **2008**, *42*, 8770–8784. [CrossRef]
21. Auvinen, M.; Boi, S.; Hellsten, A.; Tanhuanpaa, T.; Jarvi, L. Study of Realistic Urban Boundary Layer Turbulence with High-Resolution Large-Eddy Simulation. *Atmosphere* **2020**, *11*, 201. [CrossRef]
22. Giometto, M.G.; Christen, A.; Meneveau, C.; Fang, J.; Krafczyk, M.; Parlange, M.B. Spatial Characteristics of Roughness Sublayer Mean Flow and Turbulence over a Realistic Urban Surface. *Bound.-Layer Meteorol.* **2016**, *160*, 425–452. [CrossRef]
23. Landi, T.C.; Drofa, O.; Resci, G.; Roccato, F. *MOLOCH4PALM*; Institute of Atmospheric Sciences and Climate: Bologna, Italy, 2025. [CrossRef]
24. Maronga, B.; Banzhaf, S.; Burmeister, C.; Esch, T.; Forkel, R.; Fröhlich, D.; Fuka, V.; Gehrke, K.F.; Geletič, J.; Giersch, S.; et al. Overview of the PALM model system 6.0. *Geosci. Model Dev.* **2020**, *13*, 1335–1372. [CrossRef]
25. Davolio, S.; Vercellino, M.; Miglietta, M.M.; Pitura, L.D.; Laviola, S.; Levizzani, V. The influence of an atmospheric river on a heavy precipitation event over the western Alps. *Weather Clim. Extrem.* **2023**, *39*, 100542. [CrossRef]
26. Lin, D.; Zhang, J.; Khan, B.; Katurji, M.; Revell, L.E. GEO4PALM v1. 1: An open-source geospatial data processing toolkit for the PALM model system. *Geosci. Model Dev. Discuss.* **2024**, *17*, 815–845. [CrossRef]
27. Stadler, S. rPALM Code Repository. 2024. Available online: https://github.com/SebaStad/rPALM (accessed on 10 January 2025).
28. De Benedictis, C.; Nardino, M.; Cremonini, L.; Neri, L.; Fiorillo, E. Quantification of the ecosystem services provided by public and private green in a residential area of Bologna, Northern Italy. *Urban Ecosyst.* **2025**, *28*, 171. [CrossRef]
29. Lalic, B.; Mihailovic, D.T. An empirical relation describing leaf-area density inside the forest for environmental modeling. *J. Appl. Meteorol. Climatol.* **2004**, *43*, 641–645. [CrossRef]
30. Kadasch, E.; Sühring, M.; Gronemeier, T.; Raasch, S. Mesoscale nesting interface of the PALM model system 6.0. *Geosci. Model Dev.* **2021**, *14*, 5435–5465. [CrossRef]
31. Gronemeier, T.; Inagaki, A.; Gryschka, M.; Kanda, M. Large-eddy simulation of an urban canopy using a synthetic turbulence inflow generation method. *J. Jpn. Soc. Civ. Eng. Ser. B1 (Hydraul. Eng.)* **2015**, *71*, I_43–I_48. [CrossRef]
32. Wang, F.; Qin, Z.; Song, C.; Tu, L.; Karnieli, A.; Zhao, S. An Improved Mono-Window Algorithm for Land Surface Temperature Retrieval from Landsat 8 Thermal Infrared Sensor Data. *Remote Sens.* **2015**, *7*, 4268–4289. [CrossRef]

33. Malakar, N.K.; Hulley, G.; Hook, S.; Laraby, K.; Cook, M.; Schott, J. An Operational Land Surface Temperature Product for Landsat Thermal Data: Methodology and Validation. *IEEE Trans. Geosci. Remote Sens.* **2018**, *56*, 5717–5735. [CrossRef]
34. Glowienka, E.; Malinverni, E.S.; Sanità, M.; Kucza, M. Harmonizing Satellite Thermal Data with Ground-Based Observations for Climate Long-Term Monitoring. *Int. Arch. Photogramm. Remote Sens. Spat. Inf. Sci.* **2025**, *48*, 127–132. [CrossRef]
35. Olmedo, E.; Martínez, J.; Umbert, M.; Hoareau, N.; Portabella, M.; Ballabrera-Poy, J.; Turiel, A. Improving time and space resolution of SMOS salinity maps using multifractal fusion. *Remote Sens. Environ.* **2016**, *180*, 246–263. [CrossRef]
36. Morrison, W.; Grimmond, C.S.B.; Kotthaus, S.; Lindberg, F.; Onomura, S.; Sun, T. Simulating Satellite Urban Land Surface Temperatures: Sensitivity to View Angle and Landscape Complexity. *Remote Sens. Environ.* **2023**, *295*, 113640. [CrossRef]
37. Yang, J.; Menenti, M.; Wong, M.S.; Wu, Z.; Ouyang, X.; Xu, Y.; Abbas, S. Thermal Infrared Imaging of the Urban Landscape to Understand Urban Microclimate. In *Urban Remote Sensing*; Weng, Q., Quattrochi, D.A., Eds.; CRC Press: Boca Raton, FL, USA, 2021; Chapter 17; pp. 355–372. [CrossRef]
38. Rotach, M.W. Profiles of turbulence statistics in and above an urban street canyon. *Atmos. Environ.* **1995**, *29*, 1473–1486. [CrossRef]
39. Kastner-Klein, P.; Rotach, M.W. Mean flow and turbulence characteristics in an urban roughness sublayer. *Bound.-Layer Meteorol.* **2004**, *111*, 55–84. [CrossRef]
40. Christen, A.; van Gorsel, E.; Vogt, R. Coherent structures in urban roughness sublayer turbulence. *Int. J. Climatol.* **2007**, *27*, 1955–1968. [CrossRef]
41. Dupont, S.; Patton, E.G. Influence of thermal stability and seasonal canopy changes on micrometeorology within and above an orchard canopy: The CHATS experiment. *Agric. For. Meteorol.* **2012**, *157*, 11–29. [CrossRef]
42. Cava, D.; Dias-Júnior, C.Q.; Acevedo, O.; Oliveira, P.E.S.; Tsokankunku, A.; Sörgel, M.; Manzi, A.O.; de Araújo, A.C.; Brondani, D.V.; Toro, I.M.C.; et al. Vertical propagation of submeso and coherent structure in a tall and dense Amazon forest in different stability conditions PART I: Flow structure within and above the roughness sublayer. *Agric. For. Meteorol.* **2022**, *322*, 108983. [CrossRef]
43. Mortarini, L.; Dias-Júnior, C.Q.; Acevedo, O.; Oliveira, P.E.S.; Tsokankunku, A.; Sörgel, M.; Manzi, A.O.; de Araújo, A.C.; Brondani, D.V.; Toro, I.M.C.; et al. Vertical propagation of submeso and coherent structure in a tall and dense amazon forest in different stability conditions. PART II: Coherent structures analysis. *Agric. For. Meteorol.* **2022**, *322*, 108993. [CrossRef]
44. Britter, R.E.; Hanna, S.R. Flow and dispersion in urban areas. *Annu. Rev. Fluid Mech.* **2003**, *35*, 469–496. [CrossRef]
45. Barlow, J.F.; Halios, C.H.; Lane, S.E.; Wood, C.R. Observations of urban boundary layer structure during a strong urban heat island event. *Environ. Fluid Mech.* **2015**, *15*, 373–398. [CrossRef]
46. Kotthaus, S.; Grimmond, C.S.B. Energy exchange in a dense urban environment—Part I: Temporal variability of long-term observations in central London. *Urban Clim.* **2014**, *10*, 261–280. [CrossRef]
47. Dou, J.; Grimmond, S.; Miao, S.; Haung, B.; Lei, H.; Liao, M. Surface energy balance fluxes in a suburban area of Beijing: Energy partitioning variability. *Atmos. Chem. Phys.* **2023**, *23*, 13143–13166. [CrossRef]
48. Best, M.J.; Grimmond, C.S.B. Modeling the Partitioning of Turbulent Fluxes at Urban Sites with Varying Vegetation Cover. *J. Hydrometeorol.* **2016**, *17*, 2537–2553. [CrossRef]
49. Resler, J.; Krč, P.; Belda, M.; Juruš, P.; Benešová, N.; Lopata, J.; Vlček, O.; Damašková, D.; Eben, K.; Derbek, P.; et al. PALM-USM v1.0: A new urban surface model integrated into the PALM large-eddy simulation model. *Geosci. Model Dev.* **2017**, *10*, 3635–3659. [CrossRef]
50. Gaitani, N.; Spanou, A.; Saliari, M.; Synnefa, A.; Vassilakopoulou, K.; Papadopoulou, K.; Pavlou, K.; Santamouris, M.; Papaioannou, M.; Lagoudaki, A. Improving the microclimate in urban areas: A case study in the centre of Athens. *Build. Serv. Eng. Res. Technol.* **2011**, *32*, 53–71. [CrossRef]
51. Erell, E.; Pearlmutter, D.; Boneh, D.; Bar-Kutiel, P. Effect of high-albedo materials on pedestrian heat stress in urban street canyons. *Urban Clim.* **2014**, *10*, 367–386. [CrossRef]
52. Husain, S.Z.; Bélair, S.; Leroyer, S. Influence of soil moisture on urban microclimate and surface-layer meteorology in Oklahoma City. *J. Appl. Meteorol. Climatol.* **2014**, *53*, 83–98. [CrossRef]
53. Gobatti, L.; Bach, P.M.; Maurer, M.; Leitão, J.P. Impact of soil moisture content on urban tree evaporative cooling and human thermal comfort. *npj Urban Sustain.* **2025**, *5*, 26. [CrossRef]
54. Allen, L.; Lindberg, F.; Grimmond, C.S.B. Global to city scale urban anthropogenic heat flux: Model and variability. *Int. J. Climatol.* **2011**, *31*, 1990–2005. [CrossRef]
55. Flanner, M.G. Integrating anthropogenic heat flux with global climate models. *Geophys. Res. Lett.* **2009**, *36*, L02801. [CrossRef]
56. Smith, C.; Lindley, S.; Levermore, G. Estimating spatial and temporal patterns of urban anthropogenic heat fluxes for UK cities: The case of Manchester. *Theor. Appl. Climatol.* **2009**, *98*, 19–35. [CrossRef]
57. Chen, Y.; Zhou, T.; Zhang, W.; Chen, X.; Zou, L. Anthropogenic heat release increases extreme heat waves in Europe. *Clim. Dyn.* **2023**, *61*, 3831–3843. [CrossRef]
58. Liu, Y.; Wang, Y.; Li, Q.; Zhang, Y.; Zhao, L. Anthropogenic heat emissions from buildings: A review of concepts, methods, and impacts. *Atmos. Chem. Phys.* **2022**, *22*, 4721–4744. [CrossRef]

59. Cheung, P.K.; Livesley, S.J.; Nice, K.A. Estimating the cooling potential of irrigating green spaces in 100 global cities with arid, temperate or continental climates. *Sustain. Cities Soc.* **2021**, *71*, 102974. [CrossRef]
60. Asmus, C.; Hoffmann, P.; Pietikäinen, J.-P.; Böhner, J.; Rechid, D. Modeling and evaluating the effects of irrigation on land–atmosphere interaction in southwestern Europe with the regional climate model REMO2020–iMOVE using a newly developed parameterization. *Geosci. Model Dev.* **2023**, *16*, 7311–7337. [CrossRef]